

1

2

3

4

Cosmic ray validation of electrode positions in small-strip thin gap chambers for the upgrade of the ATLAS detector

5

Lia Formenti

6

7

8

Department of Physics
McGill University, Montreal
October, 2021

9

10

11

12

13

A thesis submitted to
McGill University
in partial fulfillment of the
requirements of the degree of
Master of Science

¹⁵ Table of Contents

¹⁶	1	Introduction	1
¹⁷	2	High energy particle physics	4
¹⁸	2.1	The Standard Model	4
¹⁹	2.2	Beyond the Standard Model	6
²⁰	2.3	Studying high energy particle physics with accelerators	7
²¹	3	The LHC and the ATLAS experiment	9
²²	3.1	The Large Hadron Collider	9
²³	3.2	The High-Luminosity LHC	10
²⁴	3.3	The ATLAS experiment	12
²⁵	4	The New Small Wheels	18
²⁶	4.1	Motivation for the New Small Wheels	18
²⁷	4.2	Design of the NSWs	19
²⁸	4.3	Small-strip thin gap chambers	22
²⁹	4.4	sTGC Quadruplet Construction	25
³⁰	4.5	NSW alignment	26
³¹	5	Using cosmic muons to measure relative strip position offsets	30
³²	5.1	Cosmic rays	30
³³	5.2	Experimental setup	31

34	5.3 Data acquisition	32
35	5.4 Data preparation	32
36	5.4.1 Cuts on electrode hits	32
37	5.4.2 Clustering and tracking	33
38	5.5 Measuring relative local offsets	35
39	5.6 Visualizing relative alignment between layers	38
40	5.7 Systematic uncertainty	40
41	5.8 Discussion	42
42	6 Using x-rays to measure relative strip position offsets	43
43	6.1 Experimental setup	43
44	6.2 Data acquisition	45
45	6.3 Data preparation	45
46	6.4 Measuring local offsets	47
47	6.5 Measuring relative local offsets	47
48	7 Comparing cosmic muon and x-ray relative strip position offsets	51
49	7.1 Assessing correlation	51
50	7.2 Discussion	56
51	8 Outlook and summary	58
52	8.1 Outlook	58
53	8.2 Summary	59
54	References	60
55	APPENDICES	67
56	A Cluster position uncertainty	68
57	A.1 Cluster definition	68
58	A.2 Effect of fit algorithm on cluster mean	68
59	A.3 Effect of uncertainty in cluster mean on track residuals	69

60	B Analysis statistics	70
61	C Analysis systematics	72
62	C.1 Residual distribution fit function	72
63	C.2 Cosmic muon data collection voltage	73
64	C.3 Cluster fit algorithm	75
65	C.4 Differential non-linearity	76
66	D Printable plots	79

Abstract

68 The Large Hadron Collider (LHC) is used to generate subatomic physics processes at the
69 energy frontier to challenge our understanding of the Standard Model of particle physics.
70 The particle collision rate at the LHC will be increased up to seven times its design value in
71 2025-2027 by an extensive upgrade program. The innermost endcaps of the ATLAS muon
72 spectrometer consist of two wheels of muon detectors that must be replaced to maintain
73 the muon momentum resolution in the high-rate environment. The so-called New Small
74 Wheels (NSWs) are made of two detector technologies: micromegas and small-strip thin gap
75 chambers (sTGCs). The sTGCs are gas ionization chambers that hold a thin volume of gas
76 between two cathode boards. One board is segmented into copper readout strips of 3.2 mm
77 pitch that are used to precisely reconstruct the coordinate of a passing muon. Modules of
78 four sTGCs glued together into quadruplets cover the NSWs. Quadruplets were designed
79 to achieve a 1 mrad angular resolution to fulfill the spectrometer's triggering and precision
80 tracking requirements. To achieve the required angular resolution the absolute position of
81 the readout strips must be known in the ATLAS coordinate system to within 100 μm . At
82 McGill University, the performance of sTGC quadruplets was characterized using cosmic ray
83 data before being sent to CERN, where the charge profile left by x-rays is used to measure
84 the offset of the strip patterns with respect to nominal at a limited number of points on
85 the surface of each quadruplet. The x-ray strip position measurements have acceptable but
86 limited precision and do not span the whole area of the strip layers. Given the importance of
87 knowing the absolute position of each readout strip to achieve the performance requirements
88 of the NSWs, the x-ray method must be validated by an independent method. Cosmic ray
89 data is used to characterize the relative alignment between layers and validate the x-ray
90 method.

Résumé

Le grand collisionneur des hadrons (LHC) utilise des collisions de protons afin de générer des processus de la physique subatomique à la frontière même de la haute énergie, et ceci afin de tenter remettre en cause le modèle standard de la physique des particules. Le taux des collisions entre protons au LHC sera augmenté jusqu'à sept fois le taux nominal d'ici 2025-2027 à l'aide d'un programme de mise à niveau de grande envergure. Une partie du spectromètre à muons du détecteur ATLAS consistant de deux roues de détecteurs de muons doit être remplacée afin de maintenir la résolution sur l'inertie des muons à haut taux de collision. Appelées les Nouvelles Petites Roues (NSWs), elles utilisent deux technologies de détection différentes: des chambres micromegas et des chambres à petites bandes et à intervalles fins (sTGCs). Les sTGCs sont des chambres d'ionisation de gaz, qui contiennent un volume très fin de gaz entre deux panneaux cathodiques. Un panneau est segmenté avec de petites bandes en cuivre en pente de 3.2 mm. Ceux-ci détectent le signal et permettent la mesure précise des coordonnées spatiales des muons qui traversent le détecteur. Des modules de quatre sTGCs collés ensemble en quaduplets couvrent la superficie des NSWs. Ces quaduplets ont été conçus afin de permettre une résolution angulaire de 1 mrad, et de satisfaire les exigences des systèmes de déclenchement et de mesures de précision. Afin d'atteindre cette résolution angulaire il faut que la position absolue de chaque bande soit connue au sein du détecteur ATLAS avec une précision d'au moins 100 μm . À l'Université de McGill, la performance des quaduplets a été caractériser avec des rayons cosmiques avant leur envoi au CERN, où le profil des charges laissé par des rayons X est utilisé pour mesurer le déplacement du motif des bandes par rapport à leur emplacement nominal. Ceci est fait à un nombre de positions limité sur la surface des quaduplets. Ces déplacements, mesurés pas les rayons X, ont une précision acceptable mais limitée et ne couvrent pas la région entière des panneaux. Étant donné l'importance de la caractérisation précise de la position absolue de chaque bande afin de réaliser les exigences de rendement des NSWs, il faut une méthode indépendante de validation de la méthode des rayons X est requise. Les données recueillies avec les rayons cosmiques sont utilisées pour characteriser l'alignement relatif entre les panneaux et valider la méthode des rayons-X.

Acknowledgements

- 121 Experimental particle physics projects are never done alone. I am grateful to have been
122 working with the ATLAS Collaboration for two years now.
- 123 Thank you to Dr. Brigitte Vachon for her guidance throughout this project and for editing
124 this thesis. I am consistently amazed by her ability to jump into the details of my project
125 and discuss them with me.
- 126 Thanks also to Dr. Benoit Lefebvre, who collected some of the data used in this thesis, wrote
127 several software tools I used to analyze the data and advised me several times throughout
128 this project.
- 129 Thank you to my labmates at McGill University, Dr. Tony Kwan, Kathrin Brunner, John
130 McGowan and Charlie Chen. Kathrin taught me mechanical skills that I will apply elsewhere.
131 Tony, manager of the laboratory, created the most encouraging, trusting and productive work
132 environment I have ever been apart of.
- 133 Thank you to the friends I can call on at anytime, and thank you to my family whose
134 constant support makes every step possible.

Contribution of authors

I, the author, was involved in collecting the cosmic ray data from September 2019 - March 2021. I did not design the cosmic ray testing procedure nor write the data preparation software, but I participated in using the software to analyze cosmic ray results. In the thesis, the terms “clustering,” “local offset” and “relative local offset” are defined. Cosmic ray clustering was done in the data preparation software, but I redid the fit afterwards to explore sensitivity to the fit algorithm. With help from Dr. Lefebvre and Dr. Vachon, I helped design the software that calculated the relative local offsets from cosmic ray data. I wrote that software on my own. I was not involved in the design, data collection, data preparation or analysis of the x-ray data. I also was not involved in creating an alignment model from the x-ray data. I used the x-ray local offsets calculated using x-ray data analysis software to calculate relative local offsets with x-rays. I did the comparison between the x-ray and cosmic ray data.

I hereby declare that I am the sole author of this thesis. This is a true copy of the thesis, including any required final revisions, as accepted by my examiners.

₁₅₀ **Chapter 1**

₁₅₁ **Introduction**

₁₅₂ The Standard Model (SM) is a theoretical framework that describes experimental observa-
₁₅₃ tions of particles and their interactions at the smallest distance scales; however, the questions
₁₅₄ the SM does not address motivate more experimentation.

₁₅₅ Accelerators collide particles to generate interactions that can be recorded by detectors
₁₅₆ for further study. Detectors measure the trajectory and energy of all secondary particles
₁₅₇ produced in collisions to understand the interaction. The Large Hadron Collider (LHC) [1]
₁₅₈ at CERN is the world's most energetic particle accelerator. Its energy makes it a unique
₁₅₉ tool to study elementary particles and their interactions in an environment with conditions
₁₆₀ similar to what would have existed in the early universe. If study at the energy frontier is
₁₆₁ to continue, the LHC must go on.

₁₆₂ After 2025, the statistical gain in running the LHC further without significant increase in
₁₆₃ beam intensity will become marginal. The High Luminosity Large Hadron Collider (HL-
₁₆₄ LHC) project [2] is a series of upgrades to LHC infrastructure that will allow the LHC
₁₆₅ to collect approximately ten times more data than in the initial design by \sim 2030. The
₁₆₆ increase in LHC beam intensity will result in a large increase in collision rate that will make
₁₆₇ accessible and improve statistics on several measurements of interest [3], many only possible
₁₆₈ at the LHC and the energy frontier. The increase in beam intensity will also increase the
₁₆₉ level of background radiation, requiring major upgrades to the experiments used to record
₁₇₀ the outcomes of the particle collisions.

₁₇₁ The ATLAS experiment [4] is one of the LHC's general-purpose particle detector arrays, po-
₁₇₂ sitioned around one of the collision points of the LHC. During the 2019-2022 Long Shutdown
₁₇₃ of the LHC, the most complex upgrade of the ATLAS experiment is the replacement of the
₁₇₄ small wheels of the muon spectrometer with the so-called New Small Wheels (NSWs) [5].

175 The detector upgrade addresses both the expected decrease in hit efficiency of the precision
176 tracking detectors and the high fake trigger rate expected in the muon spectrometer at the
177 HL-LHC. The NSWs are made of two different detector technologies: micromegas and small-
178 strip thin gap chambers (sTGCs). Micromegas are optimized for precision tracking while
179 sTGCs are optimized for rapid triggering, although each will provide complete coverage and
180 measurement redundancy over the area of the NSWs. Eight layers each of sTGCs cover the
181 NSWs. Practically, countries involved in detector constructor created quadruplet modules of
182 four sTGCs glued together that were arranged and installed over the area of the NSWs once
183 they arrived at CERN. Teams across three Canadian institutions built and characterized 1/4
184 of all the required sTGCs.

185 The sTGCs are gas ionization chambers that consist of a thin volume of gas held between two
186 cathode boards. One board is segmented into strip readout electrodes of 3.2 mm pitch. The
187 position of the particle track in the precision coordinate can be reconstructed from the strip
188 signals [5]. The sTGCs achieved the design track spatial resolution in the precision coordinate
189 of less than 100 μm per detector plane that will allow them to achieve a 1 mrad track angular
190 resolution using the 8 layers of sTGC on the NSW [6, 5]. The NSW measurement of the
191 muon track angle will be provided to the ATLAS trigger and used to reject tracks that do
192 not originate from the interaction point [5].

193 The precise measurement of a muon track angle depends on knowing the position of each
194 readout strip within the ATLAS coordinate system. To achieve this, the position of specific
195 locations on the surface of sTGC quadruplets will be monitored by the ATLAS alignment
196 system to account for time-dependent deformations [5]. Within a quadruplet module, the
197 strip positions could have been shifted off of nominal by non-conformities of the strip pattern
198 etched onto each cathode boards [7] and shifts between strip layers while gluing sTGCs into
199 quadruplets.

200 An xray gun was used to measure the offset of strips from their nominal position at the
201 locations that will be monitored by the ATLAS alignment system thereby providing, locally,
202 an absolute “as-built” strip position within the ATLAS coordinate system. Estimates of the
203 “as-built” positions of every readout strip are obtained by building an alignment model from
204 the available x-ray measurements [8].

205 The technique of measuring the “as-built” strip positions using xray data has never been
206 used before and must be validated. This thesis describes the use of cosmic muon data,
207 recorded to characterize the performance of each Canadian-made sTGC module, to validate
208 the x-ray strip position measurements. A description of how this work fits within the overall
209 alignment scheme of the NSW is also presented.

210 *Rewrite after implementing Brigitte’s edits.* Chapters 3 and 4 give more background on
211 particle physics, the LHC, ATLAS, the NSWs, and sTGCs. In chapter 5, the cosmic ray

212 testing procedure and how the position of the strips can be probed with cosmics data is
213 presented. Chapter 6 introduces the x-ray method, and in chapter 7, the x-ray offsets are
214 validated with cosmic muon data. The thesis concludes with a summary and outlook in
215 chapter 8.

²¹⁶ **Chapter 2**

²¹⁷ **High energy particle physics**

²¹⁸ Particle physics aims to study the elementary constituents of matter. Understanding the fun-
²¹⁹ damental building blocks and how they interact provides insight into how the early universe
²²⁰ evolved to the forms of matter we observe today. This chapter introduces general concepts
²²¹ in particle physics relevant to understanding the physics goals of the High-Luminosity LHC
²²² (HL-LHC) and NSWs upgrade.

²²³ The information on particle physics and the SM presented here is rather general; the inter-
²²⁴ ested reader is referred to [9, 10, 11] for more information.

²²⁵ **2.1 The Standard Model**

²²⁶ The Standard Model (SM) is a theoretical framework developed in the early 1970's that de-
²²⁷ scribes the observed elementary particles and their interactions. It is built on a collection of
²²⁸ quantum field theories and has been remarkably successful at predicting experimental obser-
²²⁹ vations, including but not limited to the existence of the top quark [12], the tau neutrino [13]
²³⁰ and the Higgs boson [14, 15].

²³¹ The known elementary particles described by the SM are represented in figure 2.1. There
²³² are 12 matter particles (six quarks and six leptons), 4 force-mediating particles, and the
²³³ Higgs boson. Each matter particle also has an anti-matter particle pair with the same
²³⁴ mass but opposite charge, not represented in figure 2.1. The different forces of nature are
²³⁵ understood to be the result of the exchange of force-mediating particles between interacting
²³⁶ (coupled) particles. Photons are mediators of the electromagnetic force, W⁺/- and Z bosons
²³⁷ are mediators of the weak force, and gluons are mediators of the strong force. At high

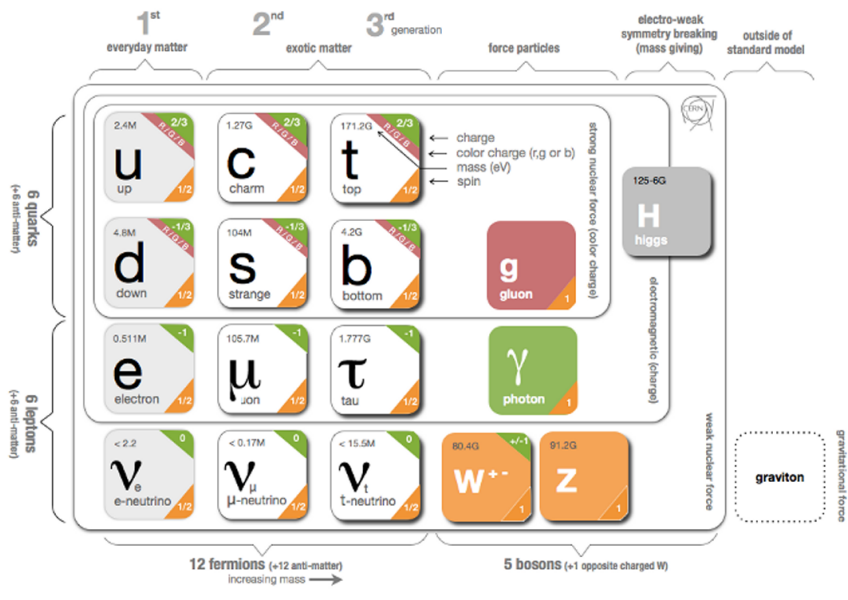


Figure 2.1: Schematic diagram of all elementary particles in the SM. Particles are grouped according to their properties and the forces through which they interact with other particles [16].

238 energy, the SM describes the electromagnetic and weak forces as stemming from a unified
239 electroweak force. The Higgs boson field interacts with the particles mediating the unified
240 electroweak force to distinguish the weak and electromagnetic forces from each other at lower
241 energies and give particles (except neutrinos) a mass. This is called electroweak symmetry
242 breaking.

243 Quarks are matter particles that are sensitive to all forces; notably they are the only particles
244 sensitive to the strong force. Protons and neutrons are made up of quarks and gluons, and the
245 strong force is responsible for their existence and mutual attraction into nuclei [17]. Leptons
246 are particles not sensitive to the strong force. Charged leptons include the electron, which
247 once part of atoms is responsible for chemistry. Of particular importance for this thesis is
248 the charged lepton called a muon. It is like the electron but its mass is \sim 200 times larger
249 than that of the electron. Muons have a lifetime of $2.2\ \mu\text{s}$ [11] and decay predominantly as
250 $\mu \rightarrow e^-\bar{\nu}_e\nu_\mu$. Neutrinos are neutral, almost massless leptons that only interact through the
251 weak force.

252 Common matter is made up of the lightest constituents of the SM: up and down quarks,
253 electrons and photons. The other particles are produced in high-energy environments but
254 then decay to the lightest constituents. Such high energy environments include the condi-
255 tions present in the early universe [18], astrophysical sources, and particle accelerators. The
256 presence of the particles of the SM at the beginning of the Universe means that their inter-
257 actions and decays are fundamental for the study of the evolution of the early universe [18].
258 Many high energy astrophysical sources, like supernovae, generate particles that rain down
259 on Earth as cosmic rays [19]. Particle accelerators have been built to create controlled en-
260 vironments of high-rate, high-energy particle collisions at high energy where the production
261 and decay of elementary particles can be directly studied.

262 **2.2 Beyond the Standard Model**

263 Despite its success at describing most experimental observations to date, there is ample
264 evidence that the SM is not a complete description of natural phenomena at the smallest
265 scales. For example, the SM has a large number of free parameters, the values of which have
266 to be fine-tuned to fit experimental observations. This is part of the so-called “naturalness”
267 problem.

268 Furthermore, the SM provides no explanation for several open questions in particle physics.
269 First, neutrinos in the SM are assumed to be massless and do not gain mass in the same way
270 as the other particles. However, neutrino were confirmed to change between their different
271 flavours in 2013 [20], which can only occur if neutrinos do have mass [21]. The neutrino

272 mass requires physics beyond the standard model [22]. Second, several astrophysical and
273 cosmological measurements suggest the presence of “dark matter” making up 85 % of the
274 matter content of the universe [23]. The nature of dark matter is unknown and so far there
275 is no SM explanation [24]. Third, the SM does not explain the origin and nature of the
276 matter-antimatter asymmetry that produced our matter-dominated universe. Finally, the
277 SM does not include a description of gravity.

278 Theoretical extensions beyond the Standard Model (BSM) aim to address some of these
279 questions, often predicting existence of yet-unseen elementary particles or physics phenomena
280 beyond those predicted by the SM. These hypothetical new physics phenomena or new
281 particles can be searched for at particle accelerators.

282 **2.3 Studying high energy particle physics with accelerators**

283

284 In particular, particle accelerators of increasingly higher energy have a long history of en-
285 abling the discovery of predicted particles. These include, for example, the discovery of
286 the W [25, 26] and Z bosons [27, 28], the top quark [29, 30], and most recently, the Higgs
287 boson [31, 32]. The discovery of the Higgs boson marked the completion of the SM as it is
288 known today.

289 Based on the established success of the SM, there are two approaches to particle physics
290 research. One approach is to search for the existence of new physics phenomena predicted
291 to exist in BSM theories and the other is to test the validity of the SM to a high degree of
292 accuracy to search for flaws in the model. Standard Model predictions are generally expressed
293 in terms of the probability of a specific physics process to occur, expressed as a cross section
294 in units of barns (with 1 barn = 10^{-28} m²). As an example, figure 2.1 shows a summary
295 of cross section measured for different physics processes using the ATLAS experiment and
296 their comparison with the predictions of the SM. Most cross section measurements agree
297 well within one standard deviation with the SM predictions.

298 Particle accelerators provide a controlled and high-collision rate environment that makes
299 them ideal places to search for new physics phenomena and to carry out systematic tests of
300 the SM. The LHC is the highest energy collider in the world so it can access physics that
301 no other accelerator can. A description of the LHC and the ATLAS detector are provided
302 in the next chapter.

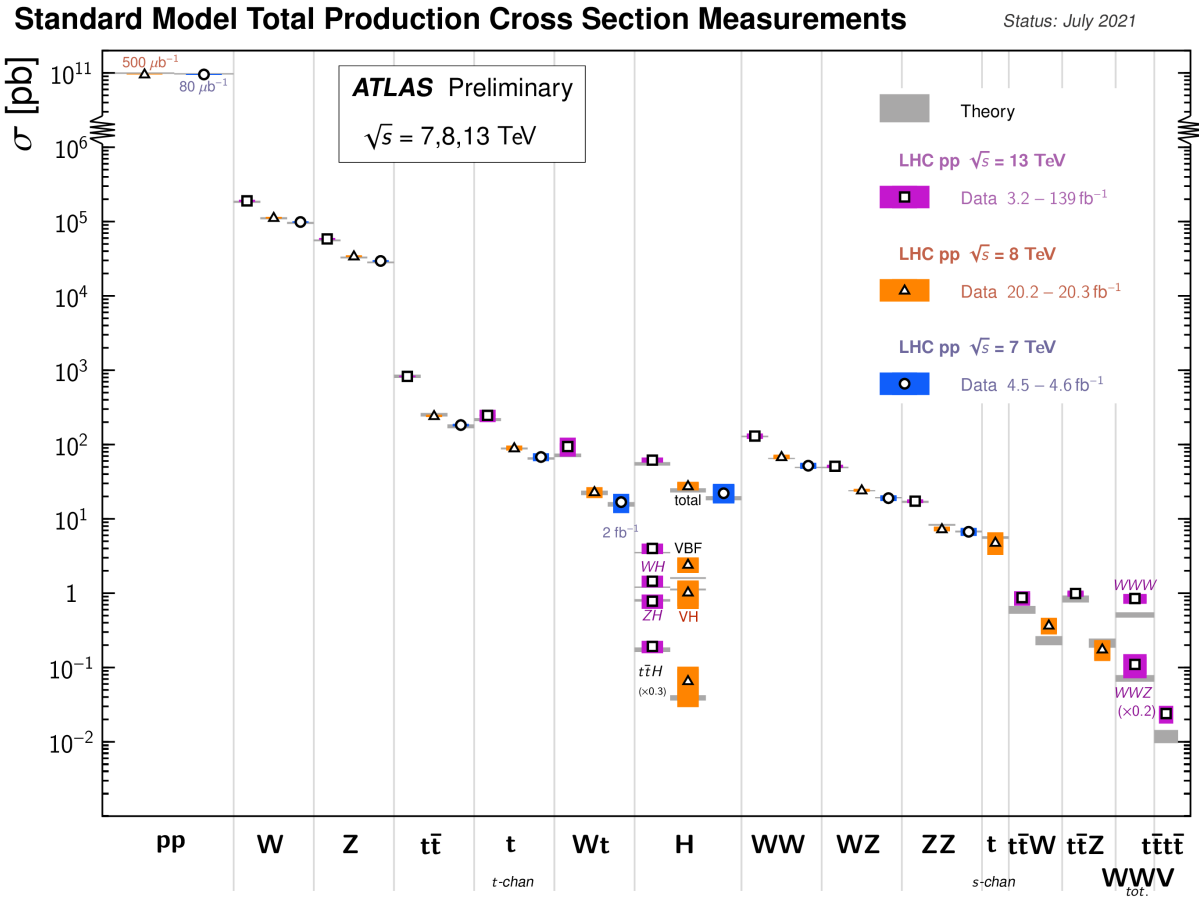


Figure 2.2: Production cross sections of different final states measured by the ATLAS experiment at the LHC. Comparison with the SM theory predictions is also shown [33].

303 **Chapter 3**

304 **The LHC and the ATLAS experiment**

305 The Large Hadron Collider (LHC) is the world's most energetic particle accelerator and the
306 ATLAS experiment is used to record the results of particle collisions at the LHC. In this
307 chapter, details about both that are necessary to understand the High-Luminosity LHC (HL-
308 LHC) upgrade project and the ATLAS experiment's New Small Wheels (NSWs) upgrade
309 are presented.

310 **3.1 The Large Hadron Collider**

311 The LHC is an accelerator 27 km in circumference and located \sim 100 m underground at
312 the CERN laboratory near Geneva, Switzerland [1]. It has two beam pipes within which
313 bunches of protons counter-circulate before being collided in the center of one of four major
314 experiments, such as the ATLAS experiment (discussed in section 3.3). Protons are guided on
315 the circular trajectory using 1232 superconducting dipole magnets capable of a maximum
316 field of 8.33 T. Radio-frequency accelerating cavities are used to accelerate protons to a
317 the maximum design energy of 7 TeV [34]. During LHC Run-1 (2011-2012), protons were
318 collided at a collision center-of-mass energy of 7 TeV and 8 TeV [35]. During LHC Run-2
319 (2015-2018), the center-of-mass energy of proton collisions was increased to 13 TeV [36],
320 close to the maximum design value of 14 TeV [34]. It is not actually the protons that
321 interact, but the constituent quarks and gluons that each carry some fraction of the energy
322 and momentum of the collisions.

323 **Luminosity**

324 The number of proton-proton interactions generated by the LHC directly affects the statistics

available to make measurements of interaction cross sections. Predicting the number of proton-proton interactions requires defining a metric called luminosity [11]. The luminosity of a particle collider is the number of particles an accelerator can send through a given area per unit time. It is calculated from the measurable quantities in Equation 3.1:

$$\mathcal{L} = \frac{f N_1 N_2}{4\pi\sigma_x\sigma_y}, \quad (3.1)$$

where f is the frequency of the bunch crossings (25 ns), N_1 and N_2 are the number of protons in each bunch ($\sim 10^{11}$ protons / bunch), and σ_x and σ_y are the RMS of the spatial distributions of the bunch. Therefore, luminosity is a property of accelerator beams, which are set by the capabilities of the accelerator. The design luminosity of the LHC was $10^{34} \text{ cm}^{-2}\text{s}^{-1}$. The units of luminosity are an inverse area; multiplying the luminosity by the cross section of a given process gives the expected rate for that process.

Integrating the *instantaneous* luminosity (equation 3.1) over a period of data collection time gives the integrated luminosity,

$$L = \int \mathcal{L}(t) dt \quad (3.2)$$

which is related to the total number of interactions. In this way, the luminosity is the link between the accelerator and the statistical power of measurements to be made with the data collected. So far, the LHC provided an integrated luminosity of 28.26 fb^{-1} in Run-1 [35] and 156 fb^{-1} in Run-2 [36].

3.2 The High-Luminosity LHC

At the end of the LHC program in 2025, the statistical gain on measurements in running the LHC further will become marginal. The HL-LHC [2] project consists of the upgrade of LHC infrastructure to achieve a nearly ten fold increase in instantaneous luminosity, thereby improving measurement statistics as well. Also, some systems will need repair and replacement to operate past ~ 2020 . The LHC will continue to be the most energetic accelerator in the world for years to come and is the only accelerator with enough energy to directly produce the Higgs boson and top quarks. Therefore, the European Strategy for Particle Physics made it a priority “to fully exploit the physics potential of the LHC” with “a major luminosity upgrade” [37]. The goal is for the HL-LHC to provide an integrated luminosity of 3000 fb^{-1} in the 12 years following the upgrade. The luminosity actually



Figure 3.1: The LHC/HL-LHC timeline [38]. The integrated luminosities collected and projected for each run of the LHC are shown in blue boxes below the timeline and the center of mass energy of the collisions is shown in red above the timeline. The top blue arrow labels the run number. The acronym “LS” stands for “long shutdown” and indicates periods where the accelerator is not operating. During the shutdowns, upgrades to the LHC and the experiments are taking place. This timeline was last updated in January, 2021, and reflects changes in the schedule due to the ongoing pandemic.

352 achieved will depend on a combination of technological advances and upgrades in progress
 353 that affect the factors contributing to luminosity defined in equation 3.1 [2]. Figure 3.1 shows
 354 the projected schedule of the HL-LHC upgrades and operation [38].

355 One of the most anticipated measurements at the HL-LHC is the value of the triple-Higgs
 356 coupling. Measuring the coupling will allow the determination of the shape of the Higgs
 357 potential responsible for electroweak symmetry breaking. Any discrepancy with respect to
 358 the SM prediction will show that there must be other sources of electroweak symmetry
 359 breaking, and hence physics phenomena beyond the SM. The LHC is the only accelerator
 360 where the Higgs boson can be produced directly so it is the only place where the triple-Higgs
 361 coupling could be measured. The HL-LHC upgrade is required to produce a significant
 362 sample of Higgs produced in pairs to make a statistically meaningful measurement [3, 39].

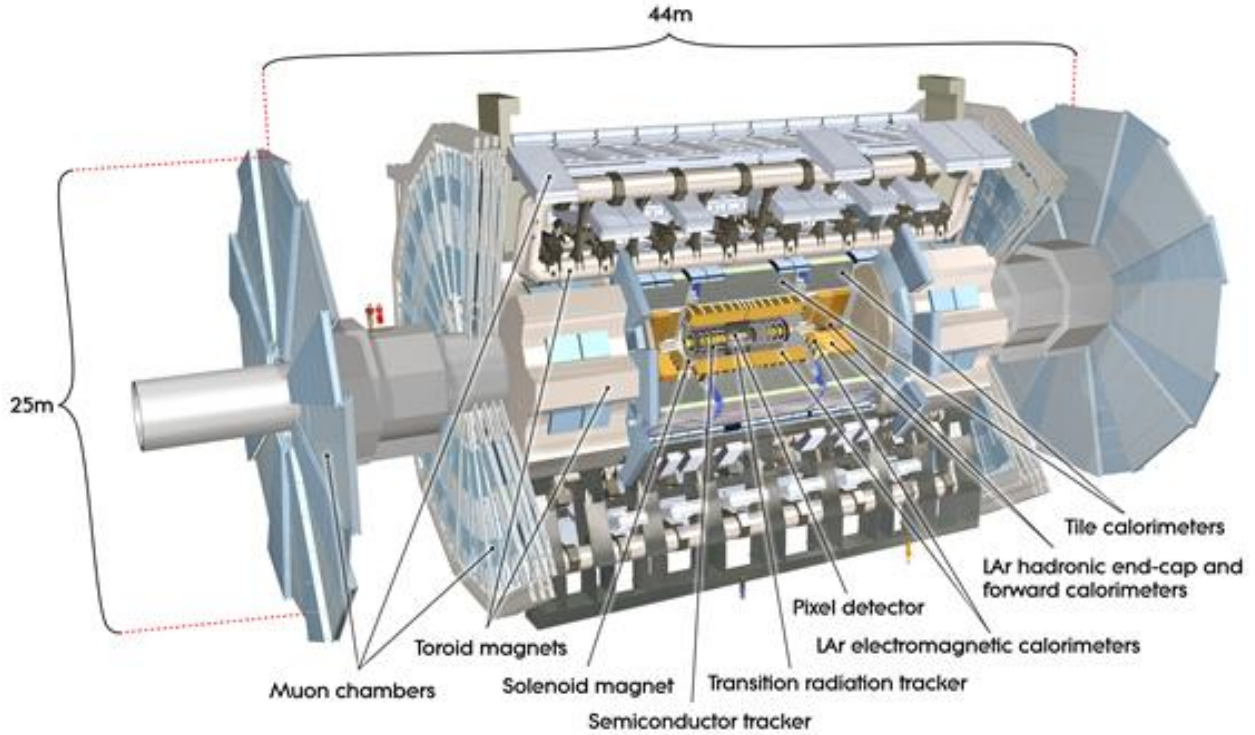


Figure 3.2: Schematic diagram of the ATLAS experiment, with the various detector subsystems labelled [4].

363 Accordingly, detector sensitivity to various Higgs decays will be important at the HL-LHC.

364 3.3 The ATLAS experiment

365 The ATLAS experiment [4] was designed to support all the physics goals of the LHC. It
366 is 44 m long and 25 m in diameter, and weighs 7000 tonnes. The ATLAS experiment is
367 centered around one of the LHC's interaction points (a place where the beams collide). As
368 shown schematically in figure 3.2, ATLAS consists of an array of particle detector subsystems
369 arranged concentrically around the beam pipe. The ATLAS experiment is cylindrical because
370 it aims to provide 4π coverage around the interaction point. In reference to the cylindrical
371 geometry of the experiment, it is helpful to separate the subsystems of ATLAS into the
372 so-called "barrel" and "endcap"/"forward" regions.

373 For analysis purposes, a spherical coordinate system is defined. The azimuthal angle ϕ is
374 measured around the beampipe and the polar angle θ is measured from the beam pipe. The
375 polar angle is more often expressed in terms of pseudo-rapidity, defined as $\eta = -\ln \tan(\theta/2)$.
376 Pseudo-rapidity values vary from 0 (perpendicular to the beam) to $\pm\infty$ (parallel to the
377 beam, defined as the z-direction) and is an approximation to the rapidity of a particle when
378 its momentum is much greater than its mass. It is useful to describe the direction of outgoing
379 particles in proton-proton collisions because differences in rapidity are invariant to a Lorentz
380 boost along the beam direction.
381 The ATLAS experiment provides identification and kinematic measurements for each particle
382 created after the initial collision, which is done by assembling offline the information recorded
383 by each subsystem. With this information, signatures of processes of interest can be identified
384 and studied. An overview of the main ATLAS subsystems is given below.

385 **The inner detector**
386 The inner detector [40, 41] (figure 3.3) is for precise measurements of charged particle tra-
387 jectories, measurement of primary and secondary interaction vertices and assistance in the
388 identification of electrons. A 2 T solenoid with field parallel to the beam bends the trajec-
389 tory of outgoing charged particles. A measurement of the bending radius of each charged
390 particle provides information about its momentum. The innermost part of the inner tracker
391 is made of high-resolution semiconductor pixel and strip detectors while the outermost part
392 is made of straw-tubes. The straw tubes are used in the trajectory measurements but they
393 are also interspersed with material designed to enhance the creation of transition radiation.
394 Transition radiation occurs when a highly relativistic charged particle traverses a material
395 boundary [42]. The amount of transition radiation emitted by a charged particle is detected
396 by the straw-tubes and is used to identify electrons.

397 **Calorimetry system**
398 Electromagnetic and hadronic sampling calorimeter units are used to record the energy
399 of electrons, photons and jets¹. A combination of liquid-argon (LAr) electromagnetic and
400 hadronic calorimeters [43] and tile-scintillator hadronic calorimeters [44] cover the rapidity
401 range $|\eta| < 4.9$, as shown in figure 3.4.
402 Sampling calorimeters have alternating layers of dense material and material that can mea-
403 sure the amount of ionization by charged particles. The dense material causes incoming

¹When quarks or gluons are expelled in a high energy collision, they create collimated groups of hadrons because they carry a charge called “colour”, and nature only allows “colourless” combinations to exist [42].

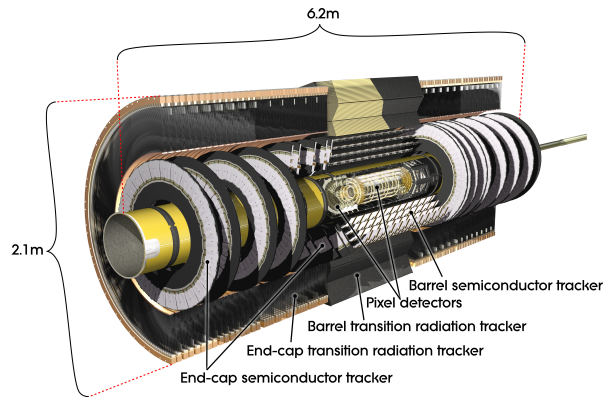


Figure 3.3: Schematic diagram of the ATLAS experiment's inner detector, with the different segments and the technology used labeled [4].

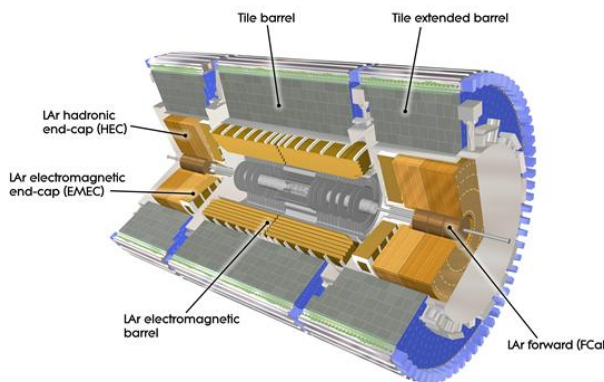


Figure 3.4: Schematic diagram of the ATLAS calorimeter system, with the different segments and the technology used labeled [4].

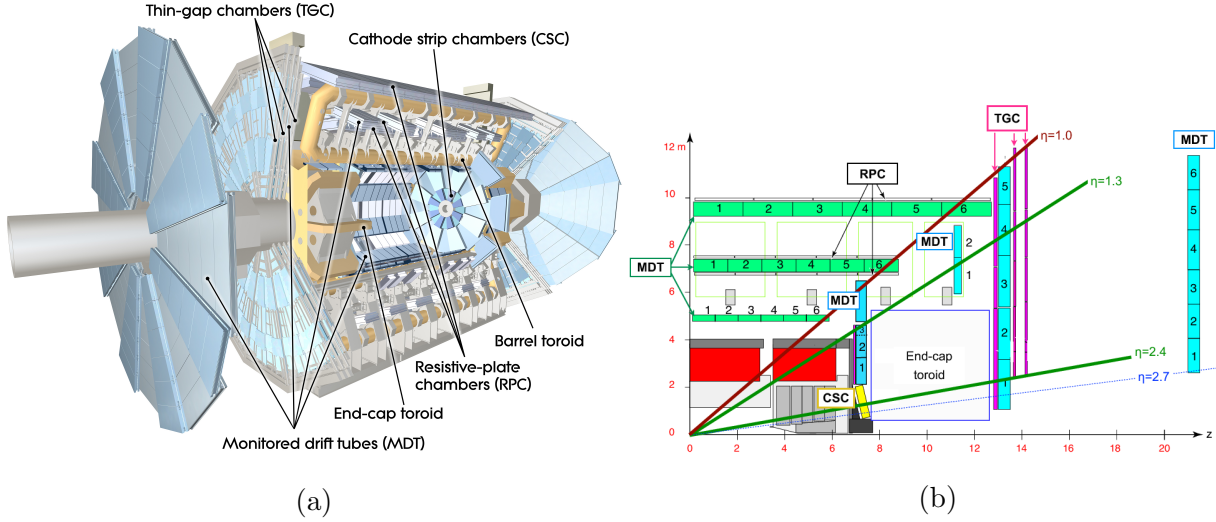


Figure 3.5: Schematic diagram of the ATLAS muon spectrometer. Figure (a) shows a 3D projection of the system with the different types of chambers and different parts of the toroidal magnet system labeled [4]. Figure (b) shows a projection of one quarter of the muon spectrometer, with the interaction point in the bottom left corner. The small wheel is just left of the end cap toroid, the big wheel is to its right, and the outer wheel is the rightmost structure [47].

404 charged particles to shower into lower energy particles and deposit their energy in the sen-
 405 sitive volume. Only muons and neutrinos are known to pass the calorimeters to the muon
 406 spectrometer without being absorbed.

407 Muon spectrometer

408 The muon spectrometer [45] consists of multiple layers of tracking chambers embedded in
 409 a 2 T magnetic field generated by an air-core superconducting toroid magnet system. Fig-
 410 ure 3.5a shows a schematic diagram of the layout of the different chambers and of the toroid
 411 magnets [4]. The trajectory of a muon is reconstructed from the information recorded by
 412 the different types and layers of tracking chambers. The amount of bending in the magnetic
 413 field provides a measure of the muon's momentum. In the barrel section of ATLAS, the
 414 toroidal magnetic field is created by eight coils bent into the shape of a "race-track" and
 415 symmetrically arranged around the beampipe. In the forward region, two end-cap toroids,
 416 each with eight smaller racetrack-shaped coils arranged symmetrically around the beam pipe
 417 are inserted in the ends of the barrel toroid [46].

418 The muon spectrometer is separated into detectors used for precision offline tracking and

419 for triggering purposes. Three layers of monitored drift tubes (MDTs) or cathode strip
420 chambers (CSCs) are used for tracking. The position of the muon track in each of the three
421 layers allows reconstruction of the bent trajectory of a muon and hence its momentum. To
422 satisfy the muon spectrometer target momentum resolution of $\Delta p_T/p_T < 1 \times 10^{-4}$ p / GeV
423 for $p_T < 300$ GeV and a few percent for lower p_T muons, the MDTs and CSCs were designed
424 to achieve a spatial resolution of 50 μm each. Accordingly, an optical alignment system was
425 designed to monitor and correct for chamber positions [45, 48].

426 Resistive plate chambers (RPCs) are used for triggering in the barrel and thin-gap chambers
427 (TGCs) are used for triggering in the endcaps. The positions of each type of chamber
428 are sketched in figure 3.5b. The endcap section of the muon spectrometer consists of three
429 sections, the small wheel, big wheel, and outer wheel – ordered by proximity to the interaction
430 point. In Run-1, low (high) p_T muons were triggered on if two (three) of the RPC or TGC
431 layers around the big wheel fired in coincidence, for the barrel and endcaps respectively [49].
432 After Run-1 it was discovered that up to 90% of the triggers in the endcap were fake, caused
433 by background particles generated in the material between the small wheel and the big
434 wheel [5]. To reduce the fake rate in Run-2, the TGCs on the inside of the small wheel also
435 had to register a hit. The added condition reduced the trigger rate by 50% in the range $1.3 < |\eta| < 1.9$ [50]. The effectiveness of the solution was limited since the $|\eta|$ -range of the small
437 wheel TGCs was limited to $1.0 < |\eta| < 1.9$ and the spatial resolution of the small wheel
438 TGCs is coarse [5].

439 Trigger system

440 It would be impossible to record all the data from bunch crossings every 25 ns, corresponding
441 to a rate of ~ 40 MHz. The ATLAS experiment has a multi-level trigger system to select
442 events of interest for permanent storage. The Level-1 (L1) hardware trigger [49] uses partial-
443 granularity information from the muon spectrometer and calorimeters to trigger on high p_T
444 muons, electrons, jets, missing transverse energy, and τ decaying to hadrons. After Run-3
445 an upgrade of the trigger system will allow a maximum trigger rate of 1 MHz with a latency
446 of 10 μs [51], but for now the working limits are a rate of 100 kHz [50] and 2.5 μs [49].

447 The L1 trigger is used to define regions of interest that are fed into the software high level
448 trigger (HLT) [52], in which the full granularity of the muon spectrometer and calorimeter
449 are used with information from the inner detector to reduce the trigger rate to 1 kHz. Events
450 that satisfy at least one of the L1 and HLT trigger criteria are recorded to permanent storage
451 for offline analysis.

453 With the foreseen increase in luminosity at HL-LHC, it is a priority to upgrade the ATLAS
454 detector to further reduce the muon trigger fake rate in the forward region. The New Small
455 Wheels being commissioned to replace the original ATLAS muon small wheels will address
456 this challenge.

457 **Chapter 4**

458 **The New Small Wheels**

459 **4.1 Motivation for the New Small Wheels**

- 460 The hit rate of all detector systems will significantly increase during HL-LHC operation
461 because of the increase in luminosity. The increased rate presents a challenge for both the
462 tracking and triggering capabilities of the muon spectrometer [5].
- 463 In terms of precision tracking, the maximum hit rate in the MDTs is expected to reach above
464 300 kHz by the end LHC operation. At this rate, the hit efficiency of MDTs decreases by
465 35%, mostly due to the long dead-time of the chambers. Losing hits in the small wheel will
466 reduce the high p_T muon momentum resolution. The decrease in resolution will affect the
467 ability to search for, for example, the decay of hypothetical heavy bosons (W' , Z') or other
468 hypothetical particles beyond the SM [3].
- 469 Already during LHC Run-2 operation, the forward muon trigger system had to cope with a
470 very high fake rate, even with the inclusion of TGC data from the small wheel as part of the
471 trigger criteria. At the luminosity expected in Run-3, it is estimated that 60 kHz out of the
472 maximum L1 trigger bandwidth of 100 kHz would be taken up by forward muon triggers.
473 To address this challenge, a possible solution would be to raise the minimum p_T threshold
474 from 20 GeV to 40 GeV. However, this would have an adverse impact on the ability to study
475 several physics processes of interest that depend on low p_T muons, particularly the Higgs
476 decay to two muons, the Higgs decay to two tau leptons and hypothetical particle decays
477 beyond the SM [5].
- 478 The NSWs will address both of these problems. They will be made of precision tracking
479 chambers suitable for the expected hit rates during the HL-LHC and triggering chambers
480 capable of 1 mrad track angular resolution. The idea behind the design triggering capability

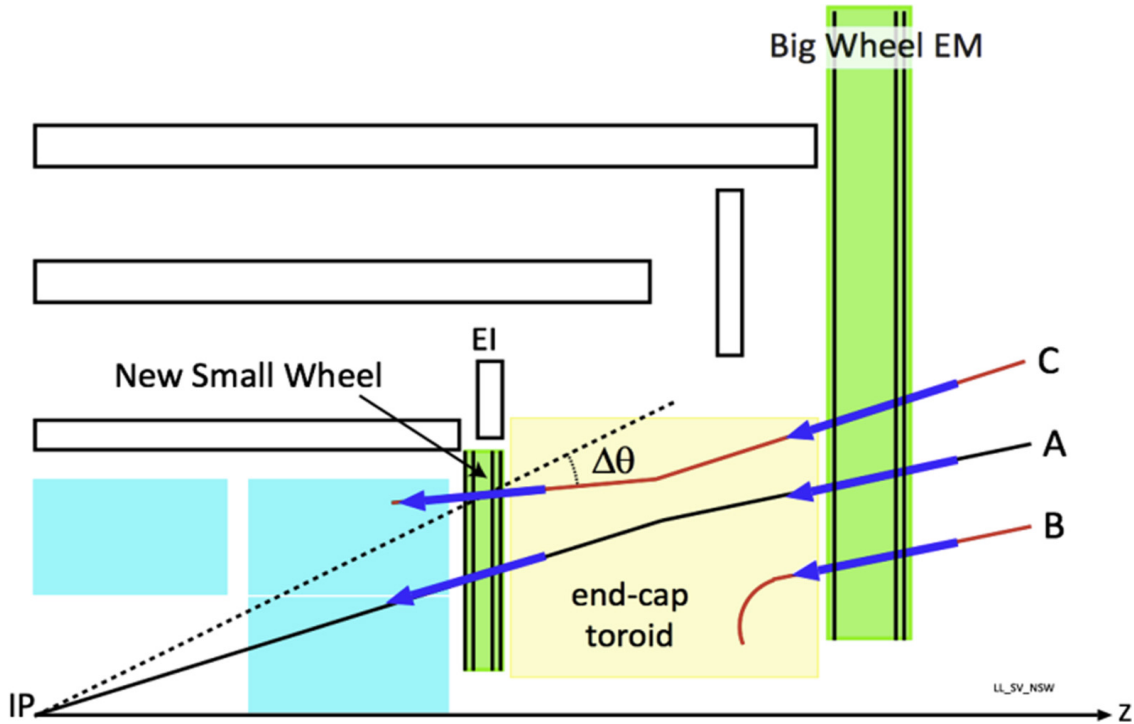


Figure 4.1: A schematic diagram of a quarter cross section of the ATLAS muon spectrometer, with the interaction point (IP) in the bottom left corner. Three possible tracks are labeled. Ideally, track A would be triggered on while track B and C discarded. With the old small wheel, all three tracks would be recorded. With the NSW, only track A would be recorded [5].

of the chambers is to allow matching of track segments measured by the NSW with track segments from the big wheel to discard tracks not originating from the interaction point. Figure 4.1 illustrates this point: the Run-2 trigger system would have triggered on all three tracks (A, B, C) while with the NSW the trigger system would only trigger on track A. The NSWs will therefore make it possible to maintain a low muon p_T trigger threshold and maintain an adequate muon momentum resolution during HL-LHC operations, which will allow the full exploitation of the physics potential of this research program [5].

4.2 Design of the NSWs

The NSWs are made with two detector technologies: micromegas and small-strip thin gap chambers. Eight layers of each cover the entire area of the wheel. Micromegas are designed

491 to be the primary precision tracking detectors and sTGCs the primary triggering detectors,
492 but both technologies offer full redundancy by being capable of providing both precision
493 measurements and trigger information. Both types of detectors were designed to achieve
494 spatial resolution better than $\sim 100 \mu\text{m}$ per layer. Four chambers are glued together to create
495 quadruplet modules of each detector type. Quadruplets of different sizes, most shaped as
496 trapezoids, are assembled into wedges. Two sTGC wedges and two micromegas wedges are
497 layered to create sectors (with the sTGC wedges on the outside) [5]. Different stages of the
498 construction process are shown in figure 4.2. At the time of writing, the assembly of the
499 NSWs has just been completed. The first NSW has been lowered into the ATLAS cavern
500 and is being commissioned and the second will be lowered shortly.



(a) A sTGC quadruplet module. The left image highlights the trapezoidal shape of a quadruplet module. The right image shows the corner at the short edge, where the four sTGC layers and each layer's gas inlet are visible. The gas outlets and high voltage cables are located along the long edge near the corner in the back left of the photo. The green printed circuit board along the sides are the adaptor boards where the front end electronics are attached.



(b) Left: A sTGC wedge. The white frame outlines the individual quadruplet modules that have been glued together into a wedge. Right: A completed sector, with two sTGC wedges on the outside and two micromegas wedges on the inside.



(c) A picture of one of the two NSWs. All sectors except one large sector at the top are installed, revealing two of the smaller sectors that are normally hidden under the large sectors and support bars. The NSWs are 9.3 m in diameter.

Figure 4.2: Images showing different stages of NSW construction.

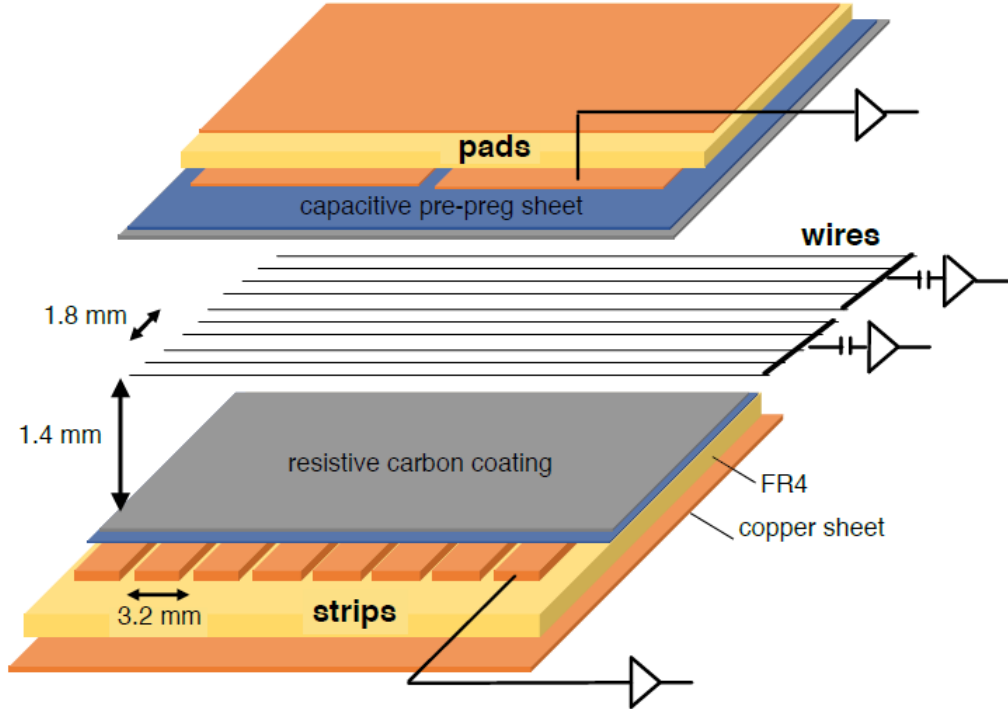


Figure 4.3: Internal structure of an sTGC, zoomed into the area under a pad. High voltage is applied to wires suspended in the gas volume to create an electric field. A passing muon causes an ionization avalanche that is picked up by the wire, strip and pad electrodes [8].

501 4.3 Small-strip thin gap chambers

502 The sTGCs are gas ionization chambers operated with a gas mixture of CO₂:n-pentane with
 503 a ratio of 55%:45% by volume. Gold-plated tungsten wires, 50 µm in diameter and with
 504 1.8 mm pitch, are suspended between two cathode planes made of FR-4, each 1.4 mm away
 505 (see figure 4.3). One cathode board is segmented into copper pads of varying area (with a
 506 typical size of $\sim 300 \text{ cm}^2$ each), and the other is segmented into copper strips of 3.2 mm pitch
 507 running lengthwise perpendicular to the wires. High voltage is applied to the wires and the
 508 cathode planes are grounded [5, 53]. When a muon passes through a sTGC, it will ionize
 509 some of the atoms in the gas and the electric field in the gas gap will result in the formation
 510 of an ionization avalanche [54]. The motion of the ions and free electrons generates small
 511 currents on the nearby wire and capacitatively-coupled strip and pad electrodes [5]. The gas

512 mixture was chosen to absorb excess photons produced in the avalanche that delocalize the
513 avalanche signal [55] preventing the formation of streamers [42]. This allows the chamber to
514 be run at a higher high-voltage providing a faster response and higher signal. The resistivity
515 of the carbon coating and capacitance of the pre-preg sheet tune the spread of the charge
516 distribution [56] and the speed of the response [57] to optimize the rate capability. The
517 combined information from the strip readout electrodes and wires provide the location where
518 the muon passed through the chamber. The small pitch of the strip readout electrodes is
519 what allows the quadruplets to deliver good track angular resolution to improve the fake
520 trigger rate and meet the precision tracking requirements [5].

521 A 3-out-of-4 coincidence in pad electrodes from each layer of a quadruplet defines a region of
522 interest where the strip and wire electrodes should be read out. The pad triggering scheme
523 greatly reduces the number of electrodes that require readout so that a track segment of the
524 required angular resolution can be provided quickly enough to the hardware trigger [5].

525 Signal is read out from groups of successive wires, so the position resolution in the direction
526 perpendicular to the wires is 10 mm per plane. The wires give the azimuthal coordinate
527 in ATLAS so the position resolution in this direction is sufficient. Good resolution on the
528 η coordinate, perpendicular to the strips, is important [5]. In a test beam environment,
529 the strip spatial resolution of a single sTGC was measured to be 45 microns for muon
530 perpendicularly incident on the surface of the sTGC. Although the spatial resolution worsens
531 as function of muon angle measured from normal incidence [58], when four sTGCs are glued
532 together into a quadruplet the design angular resolution of 1 mrad in the strip coordinate is
533 achievable [5, 53].

534 To achieve the required track angular resolution once installed in ATLAS, the absolute
535 position of each sTGC strip within the ATLAS coordinate system must be accurately known.
536 The degree of accuracy required is on the order of the position resolution of the chambers,
537 $\sim 100 \mu\text{m}$. The NSW alignment system, detailed in section 4.5, will monitor the position of
538 alignment platforms installed on the surface of the wedges. The alignment platforms are
539 installed with respect to an external reference on the sTGCs: two brass inserts on each strip
540 layer on one of the angled sides of each quadruplet (shown in figure 4.4). So the challenge
541 of monitoring the position of the strips in ATLAS was separated into two steps: first, infer
542 the position of the strips with respect to the brass inserts using the sTGC design geometry;
543 second, use the alignment system to monitor the position of the alignment platforms. The
544 next section provides some pertinent details on the sTGC construction process, with steps
545 that affect the position of the strips with respect to the brass inserts highlighted.



(a) Brass insert near long edge.

(b) Brass insert near short edge.

Figure 4.4: The brass inserts sticking out from the gas volumes of an sTGC quadruplet. These inserts were pressed against alignment pins when the individual sTGCs were being glued together.

546 4.4 sTGC Quadruplet Construction

547 Five countries were responsible for producing sTGC quadruplets of varying geometries for the
548 NSW: Canada, Chile, China, Israel and Russia. Canada was responsible for the construction
549 of one quarter of the required sTGCs, of three different quadruplet geometries. The steps of
550 the construction process in each country were similar [5]. The process followed in Canada is
551 detailed here.

552 A research group at TRIUMF in Vancouver, British Columbia was responsible for preparing
553 the cathode boards. The boards were made and the electrodes etched on at a commercial
554 laboratory, Triangle Labs, in Carson City, Nevada. Once completed they were sent to TRI-
555 UMF to be sprayed with graphite and to have support structures glued on [7]. The boards
556 are commercial multilayer printed circuit boards, but the strip boards required precision ma-
557 chining to etch the strip pattern [5]. Triangle Labs also machined the two brass inserts into
558 each strip board. A coordinate measuring machine (CMM) was used to accurately measure
559 the position of a set of reference strips on each board. Four quality parameters describing
560 non-conformities in the strip pattern of each board with respect to the brass inserts were
561 derived from the data and the results are available on a QA/QC database. The parameters –
562 offset, angle, scale and nonparallelism – and the CMM data collection is described in full
563 in [7]. Due to time constraints, tolerances on the non-conformities in the etched strip pattern
564 with respect to the brass inserts were loosened, with the condition that the strip positions
565 in ATLAS would have to be corrected for [7].

566 The prepared boards were sent to Carleton University in Ottawa, Ontario for construction
567 into sTGCs and quadruplets. First, the wires were wound around the pad cathode boards
568 using a rotating table and the wires were soldered into place. A wound pad cathode board glued
569 on top to create an sTGC. Holding one sTGC flat with the vacuum, another was glued on
570 top to create a doublet, then two doublets were glued together to create a quadruplet. When
571 gluing sTGCs together, the brass inserts were pushed against alignment pins with the goal of
572 keeping the strip layers aligned within tolerance. However, non-conformities in the shape of
573 the brass inserts, non-conformities in the position of the alignment pins and shifts between
574 sTGCs while the glue cured resulted in misalignments between the brass inserts and strip
575 layers. Precise alignment of the pad boards or wires with respect to the strip boards did
576 not have to be so tightly controlled because pads and wires do not measure the precision
577 coordinate.

579 The Carleton team finished the quadruplets by installing adaptor boards on the angled sides
580 of each layer that allow front end electronics to be attached. Completed quadruplets were
581 sent to McGill University where their performance was characterized with cosmic rays. De-

582 tails pertaining to cosmic ray testing of sTGC quadruplets at McGill University are described
583 in chapter 5. Tested quadruplets were sent to CERN where they were assembled into wedges
584 and alignment platforms installed. The alignment platforms were installed using a jig posi-
585 tioned with respect to the brass inserts. Completed wedges were assembled into sectors then
586 installed on the NSWs.

587 The quadruplet construction process had two steps where strip positions could be shifted off
588 of nominal. At board-level, there could be non-conformities in the etched strip pattern with
589 respect to the brass inserts, described by the four quality parameters [7]. At the quadruplet
590 level, misalignments between the brass inserts and strips on different layers were possibly
591 introduced during the gluing. The result was that the brass inserts were not a reliable
592 reference point and that the strips can be offset from their design position by up to hundreds
593 of micrometers. Offsets in strip positions from nominal in Canadian quadruplets were shown
594 to be random [7], so no one correction would suffice. The offsets must be measured and
595 corrected for in the ATLAS offline software that does the precision tracking. Understanding
596 the work ongoing to make measurements of strip position offsets and correct for them requires
597 understanding the strategy of the NSW alignment system.

598 4.5 NSW alignment

599 The idea of the NSW alignment system is presented in [5], but the details have only been
600 presented internally so far. After the wedges are constructed, alignment platforms are in-
601 stalled on every sTGC quadruplet and optical fibres routed to them, as shown in figure 4.5.
602 Light from the optical fibres will be monitored in real time by cameras (BCAMs) mounted on
603 the alignment bars of the NSWs. The system will thus record the positions of the alignment
604 platforms in the ATLAS coordinate system and any changes over time.

605 The original alignment scheme was to use the brass inserts as a reference between the align-
606 ment platforms and the individual strips, as shown in the solid arrows in figure 4.6 – this
607 will no longer work. The position of the alignment platforms will be known thanks to the
608 alignment system, so a different method to get the position of the strips with respect to the
609 alignment platforms is currently in its final stage of development. The technique consists of
610 the measurement of the strip pattern offset at a few areas on the surface of a sTGC quadru-
611 plet using an xray gun mounted on the alignment platforms. The local strip pattern offset
612 with respect to nominal geometry at the location of each alignment platform is obtained
613 by analyzing the xray gun beam profile. As shown in figure 4.6, this approach essentially
614 bypasses the need to know the position of strips with respect to the brass inserts. The align-
615 ment platforms provide the link to the nominal geometry because the nominal group of strips

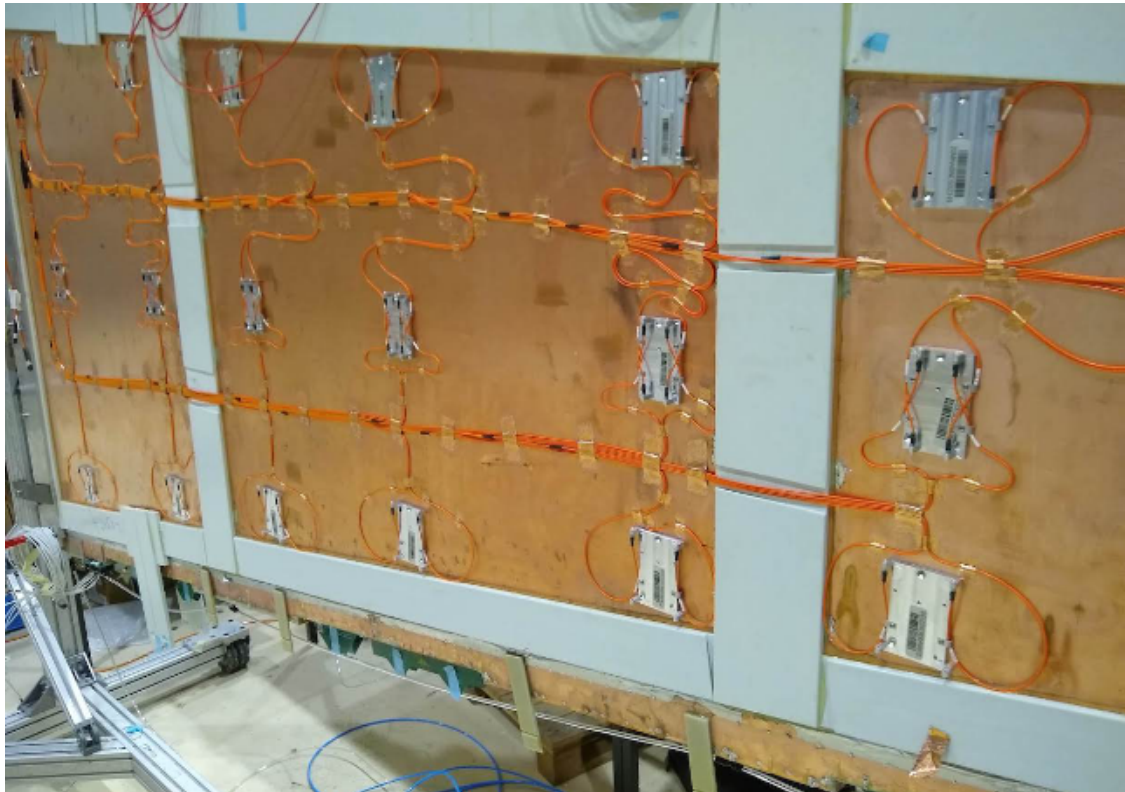


Figure 4.5: A sTGC wedge with alignment platforms (silver) installed on the quadruplet. Optical fibres (orange) are routed to the alignment platforms. Cameras on the frames of the NSWs will record light from the optical fibres to monitor in real-time the position the alignment platforms in the ATLAS coordinate system.

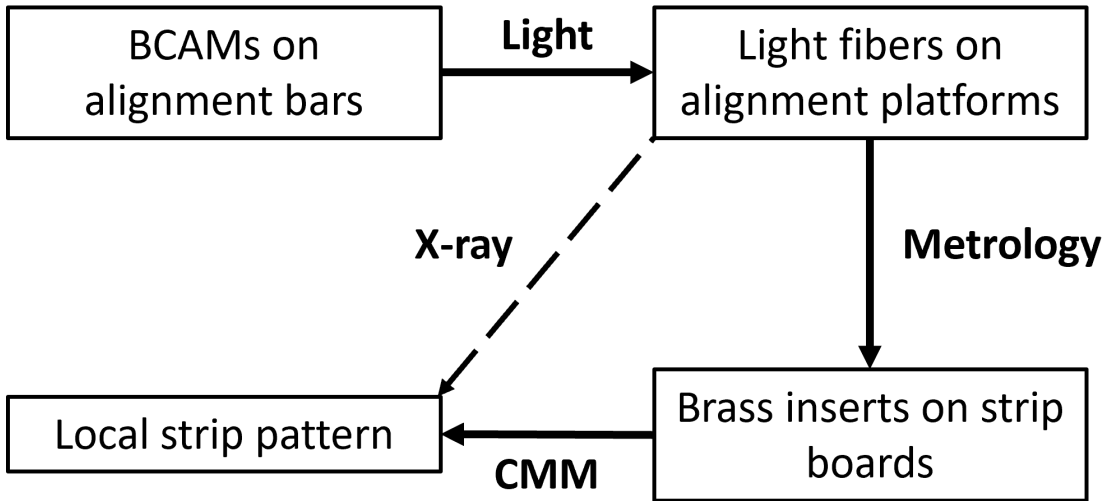


Figure 4.6: Schematic diagram showing how the different elements of the sTGC alignment system relate to one another. The solid arrows denote the planned alignment scheme. The dashed arrow shows the modification being finalized now. This figure was originally designed by Dr. Benoit Lefebvre.

616 that should be nearest to them can be identified using the nominal geometry parameters that
 617 assume the strips are perfectly etched and aligned. Cosmic muon track positions cannot be
 618 compared to the nominal geometry because the alignment platforms are not installed when
 619 cosmics data is collected, so there is no external reference to provide a link to the nominal
 620 geometry.

621 The x-ray method does not have the sensitivity to measure the offset of each strip from
 622 nominal, but what can be measured instead is the offset of the strip pattern in a local area
 623 around the position of the gun. *Local offsets* are used to build an alignment model for each
 624 strip layer. Formally defined, an alignment model is a set of parameters used to estimate the
 625 “as-built” position of a strip given its nominal position. The alignment model currently being
 626 worked on takes x-ray and CMM data as input to calculate an overall offset and rotation of
 627 each strip layer with respect to nominal [8]. The alignment parameters could be described
 628 as “global”, meaning over the whole layer instead of local. Without the x-ray dataset, there
 629 would be no input to the alignment model that takes into account inter-layer misalignments
 630 introduced during quadruplet construction.

631 Given that the x-ray local offsets can only be measured at positions where the gun can
 632 be attached and that they are an important part of the alignment scheme, the new x-ray
 633 measurement technique needs to be validated. The goal of this thesis is to validate the x-ray

⁶³⁴ local offsets while exploring how cosmics data complements and adds to the understanding
⁶³⁵ of strip positions and global alignment.

636 Chapter 5

637 Using cosmic muons to measure 638 relative strip position offsets

639 At McGill, among other quality and functionality tests, each Canadian-made quadruplet was
640 characterized with cosmic muons. In this chapter, the experimental setup and how the data
641 was analyzed to provide relative strip position offsets is presented. The analysis method
642 was motivated by the how it could be compared to data collected with the x-ray method
643 (chapter 6) but also stands alone as a characterization of the alignment between strips of
644 different layers. First, a brief introduction to cosmic rays.

645 5.1 Cosmic rays

646 The Earth is being bombarded by particles from the sun, galactic sources and extra galactic
647 sources – collectively called cosmic rays [19, 11]. Cosmic rays are mostly protons, but also
648 heavier ions, gamma rays and the term sometimes includes neutrinos. The primary (initial)
649 cosmic ray interacts with the atmosphere causes electromagnetic and hadronic showers of
650 particles. Hadronic showers result from the primary cosmic ray interacting strongly with the
651 target of the atmosphere and the most abundant products are pions. Charge pions mostly
652 decay to muons (there is a lesser contribution to the muon flux from kaons as well) [59].
653 Thanks to time dilation extending the muon’s lifetime as measured on Earth, a flux of
654 approximately 1 muon/cm²/ min reaches the ground [11]. Measuring the muon flux and
655 energy spectrum reveals information about primary cosmic rays [59] which is interesting to
656 high energy physicists and astrophysicists. The muon flux is also terribly convenient for
657 testing muon detectors.

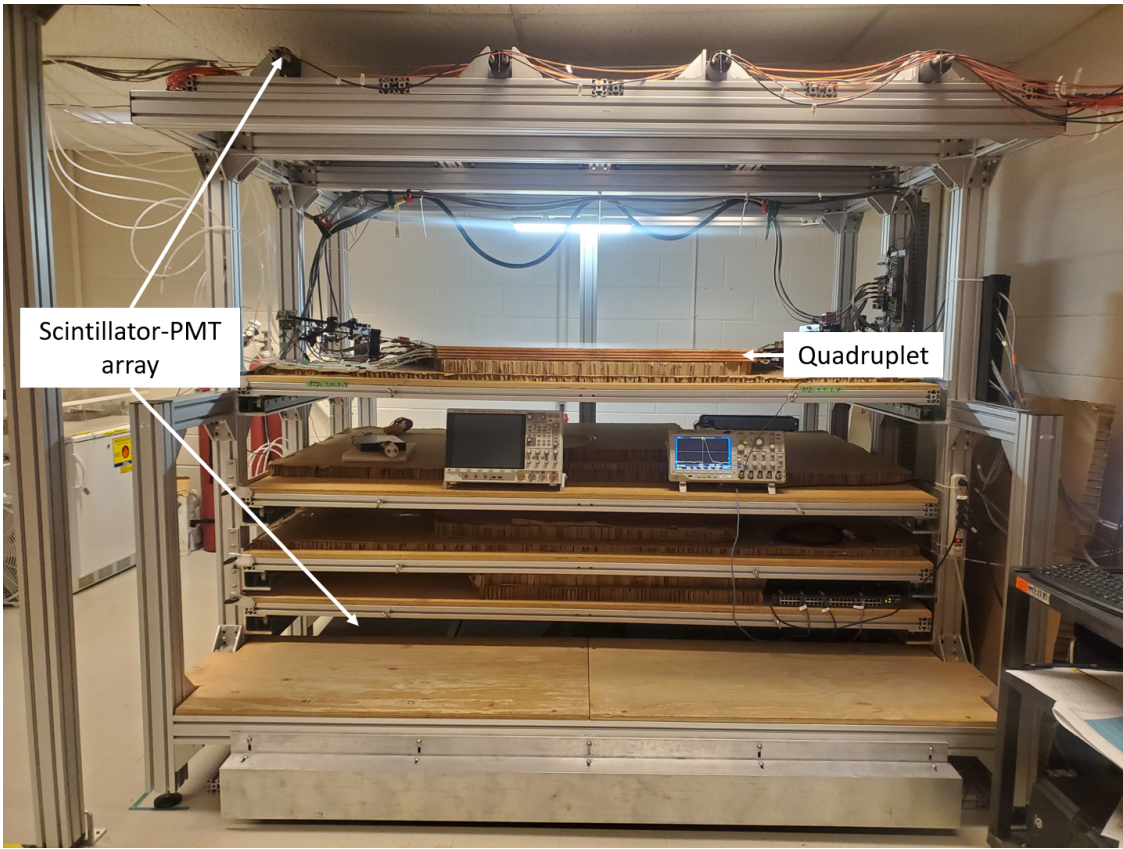


Figure 5.1: Cosmic muon hodoscope at McGill University with sTGC quadruplet in the test bench.

658 5.2 Experimental setup

659 Cosmic muon characterization was done with a hodoscope, a complete description of which
 660 can be found in [58]. The quadruplet was placed in the center of the test bench. Above
 661 and below it was a layer of scintillator-PMT arrays, labeled in figure 5.1. When a cosmic
 662 muon passed within the acceptance of the hodoscope, at least one scintillator from the top
 663 array and at least one from the bottom array fired in coincidence. The coincident signal was
 664 used to trigger the readout of the quadruplet's electrodes using NIM modules. The trigger
 665 was passed to the front-end electronics attached to the adaptor boards of each layer of the
 666 quadruplet.

667 Operating the chambers also required gas and high voltage. A pentane-CO₂ mixture was
 668 mixed and delivered to each sTGC with a gas system designed and made at McGill University.

669 The gas system was controlled by a slow control program, also made in-laboratory [60].
670 Although gas mixture is flammable, it allows the chambers to operate in high amplification
671 mode without production of excess photons saturating the signal across many strips because
672 pentane absorbs a wide energy of photons [55]. To prepare the quadruplets for operation,
673 CO₂ was flushed through them overnight to remove impurities. Then, five gas volumes of
674 the pentane-CO₂ mixture was flushed through (approximately 3 hours). High voltage was
675 provided by CAEN boards.

676 5.3 Data acquisition

677 Each sTGC electrode was connected to a channel on a prototype ASIC¹ on the front-end
678 electronics, attached to the adaptor boards on each layer of a quadruplet. The ASIC ampli-
679 fied the signal and was set to measure and record the signal peak amplitude from electrodes.
680 For each trigger, the signal peak amplitude of all channels above threshold was recorded
681 as an event and stored in a binary file. Channel thresholds were estimated [62] and ad-
682 justed manually in the configuration/readout software before the start of data acquisition.
683 There was an exception to the threshold rule: the signals on strips adjacent to a strip above
684 threshold were also readout using the so-called “neighbour triggering” function of the ASIC.
685 The quadruplets were held at 3.1 kV for approximately two hours to collect data from 1
686 million muon triggers.

687 5.4 Data preparation

688 5.4.1 Cuts on electrode hits

689 Corrupted data is removed while the raw data is being recorded in a binary file. The binary
690 file is decoded into a usable ROOT [63] tree offline.
691 A hit is defined as a signal recorded from a channel that was above threshold or (in the
692 case of strips) neighbour triggered. In addition to hits from muons, the quadruplets record
693 noise from the electronics and δ -rays (electrons liberated with sufficient energy to cause more
694 ionization before acceleration). Therefore, cuts are applied to reduce the number of noise
695 hits. The edge strips are very noisy, so all strip hits on layers with strip hits on either
696 edge channel are cut. A default pedestal value is subtracted from the recorded signal peak

¹the VMM3 [61], designed for the MMs and sTGCs of the NSW

697 amplitude of each electrode for a more realistic estimate of the signal amplitude. Also, events
698 that only have hits on pad electrodes (no strips or wires) were cut because the large area of
699 the pads made them susceptible to noise.

700 **5.4.2 Clustering and tracking**

701 Many of the high-level characterization metrics require rebuilding muon tracks. For events
702 passing quality cuts, the x - and y -coordinates of the ionization avalanche on each layer are
703 extracted from the signal on the wires and strips respectively for each event, as is sketched in
704 figure 5.2. In this work, x is the coordinate perpendicular to the wires and y is the coordinate
705 perpendicular to the strips.

706 The x -coordinate is taken as the center of the wire group with the maximum peak signal
707 amplitude, since the wire groups' pitch (36 mm) is larger than the typical charge spreading.
708 Assuming that the true x -position of the hit is sampled from a uniform distribution over the
709 width of the wire group, the uncertainty in the x -position was given by $\frac{36}{\sqrt{12}}$ mm = 10 mm [64].

710 The y -coordinate is taken as the Gaussian mean of the peak signal amplitude distribution
711 across groups of contiguous strips. The process of grouping contiguous strip hits on a layer is
712 called clustering, and the resulting group is called a cluster. Figure 5.2 sketches the clustering
713 process and a sample cluster is shown in figure 5.3. The data acquisition system recorded
714 the electrode ID of the strip hit and in the clustering process the position of the center
715 of the strip electrode is calculated based on the nominal quadruplet geometry. Typically,
716 clusters are built of 3-5 strips. The thickness of the graphite coating over the cathode boards
717 determined how many strips picked up the ionization image charge. Larger clusters were
718 more likely caused by δ -rays since they spread the cloud of ionization.

719 Events are cut from the analysis if there are two clusters on one layer's set of strips (indicative
720 of noise). Clusters are cut if the cluster size is lesser than three (which should not happen for
721 real events thanks to neighbour triggering), and if the cluster size is greater than 25. After
722 all the cuts on hits and clusters, roughly half as many muon tracks as triggers collected
723 remain.

724 The uncertainty in the y -coordinate could have been taken as the fitted cluster mean's
725 statistical uncertainty; however, after comparing the difference in cluster means for different
726 fitting algorithms in appendix A.2, 60 μm of uncertainty was assigned.

727 The coordinates of the avalanches' on all layers were used to reconstruct tracks in x and y
728 respectively. The tracks were then used to calculate characterization metrics like electrode
729 efficiency and spatial resolution, the details of which are discussed in [58].

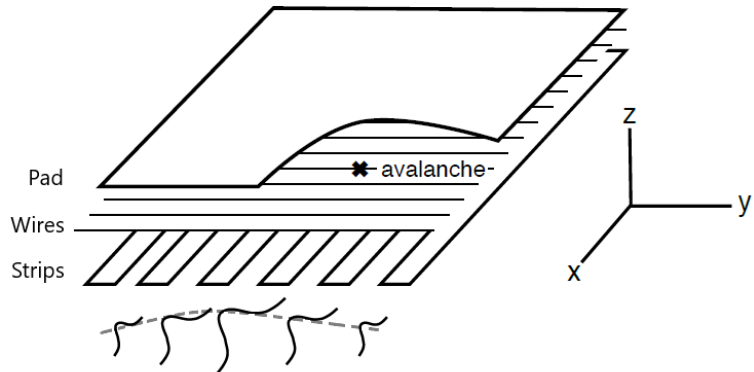


Figure 5.2: A sketch of an sTGC-like detector. The position of the avalanche is extracted from the wires and strips that picked up the avalanche signal. The signals on individual strips are sketched. Clustering was the processs of fitting a Gaussian to the peak value of the signals on individual contiguous strips, as is done in figure 5.3. In this work, the $x(y)$ -coordinate will always refer to the coordinate perpendicular to the wires (strips) [58, 56].

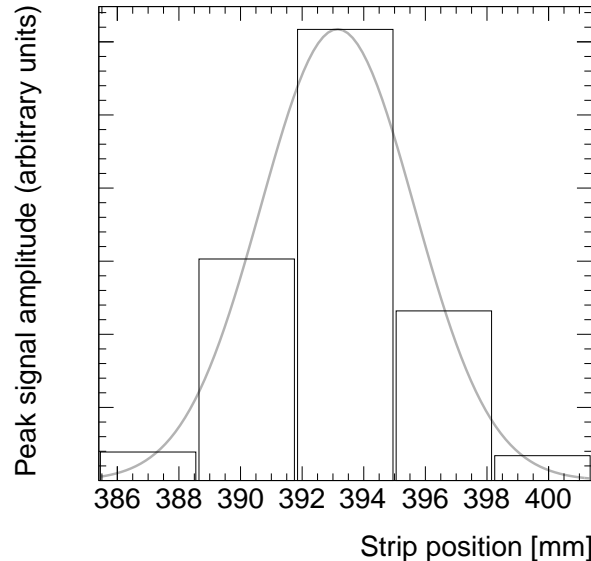


Figure 5.3: A sample cluster resulting from the current picked up on a group of strips after the passing of a muon (presumably). The grey curve is a Gaussian fit.

730 5.5 Measuring relative local offsets

731 The offset of a strip from its nominal position can be modeled as a passive transformation.
732 For each area of a strip layer, the local offset is the shift of the strip pattern in that area with
733 respect to the nominal geometry. Local offsets systematically change the set of strips nearest
734 to muons passing through the area. The data preparation software assumes that strips are
735 in their nominal positions, so the recorded muon y -position on layer i , y_i , is shifted opposite
736 to the layer's local offset, $d_{local,i}$, by

$$y_i = y_{nom,i} - d_{local,i}, \quad (5.1)$$

737 where $y_{nom,i}$ is the position of the muon that would have been recorded on layer i if there
738 was no local offset. Equation 5.1 ignores other factors that affect the cluster position, like
739 position resolution. With cosmics data, the local offset is unknown and there was no external
740 reference to measure $y_{nom,i}$. Therefore, only relative local offsets could be calculated.

741 The minimal relative coordinate system uses two reference or fixed layers [58]. The hits
742 on the two fixed layers were used to create tracks that can be interpolated or extrapolated
743 (polated) to the other two layers. The set of two fixed layers and the layer polated to are
744 referred to as a tracking combination. The residual of track i , Δ_i is defined as,

$$\Delta_i = y_i - y_{track,i}, \quad (5.2)$$

745 where $y_{track,i}$ is the polated track position. Track residuals are affected by the relative local
746 offset in the area of each layer's hit. As an example, in figure 5.4, the residual on layer
747 2 perhaps indicates that layer 2 is offset with respect to layers 1 and 4 in the area of the
748 track. Of course, a single track residual says nothing of the real relative local offset because
749 of the limited spatial resolution of the detectors and fake tracks caused by noise or delta
750 rays. However, the mean of residuals for all tracks in a region will be shifted systematically
751 by the local offsets between layers [58]. For a quadruplet with nominal geometry, the mean
752 of residuals should be zero in all regions and for all reference frames, unlike the example
753 regions in figure 5.5. The value of the mean of residuals is a measure of the relative local
754 offset of the layer with respect to the two fixed layers. The sign convention is such that the
755 mean of residuals is opposite to the relative local offset.

756 To study the relative local offsets, residual distributions across each strip layer of a quadruplet
757 for all tracking combinations were assembled and fitted. The residual distributions were
758 wider for tracking combinations where the extrapolation lever arm was largest, as in the
759 example distributions shown in figure 5.5. In general, residual means from distributions of
760 residuals with geometrically less favourable tracking combinations have larger statistical and

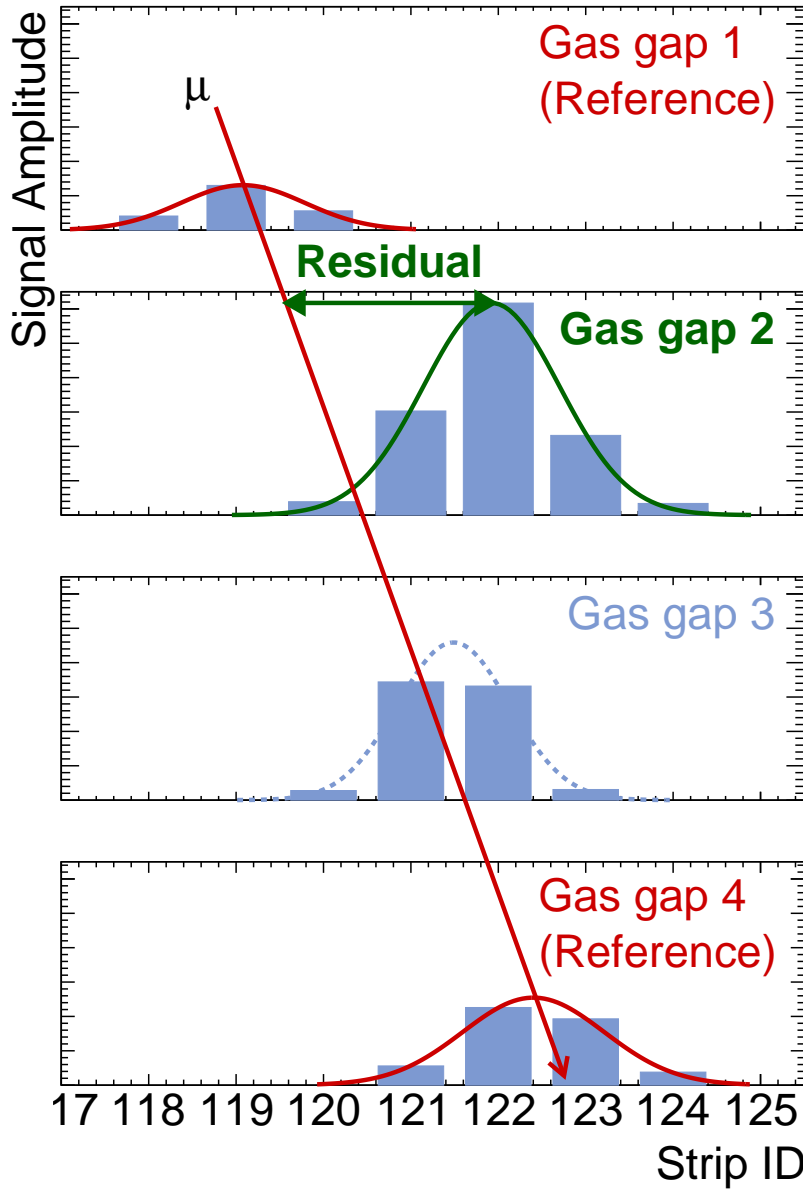
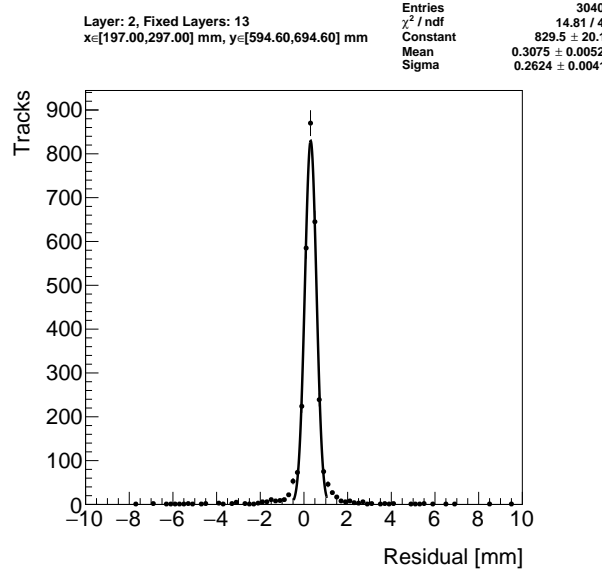
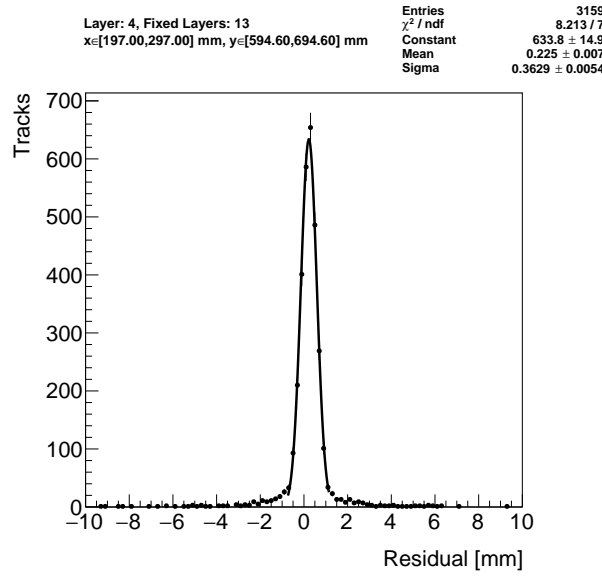


Figure 5.4: Representation of a muon event recorded by an sTGC. The clusters are fit with a Gaussian and the mean is taken as the hit position. A track is built from the chosen reference layers, 1 and 4, and the residual calculated on layer 2. The clusters come from a real muon, but their positions were modified to highlight the residual on layer 2.



(a) Tracks on layer 2, reference layers 1 and 3.



(b) Tracks on layer 4, reference layers 1 and 3.

Figure 5.5: Residual distribution in the region $x \in [197, 297]$, $y \in [594.6, 694.6]$ mm (100 mm by 100 mm area) for two different tracking combinations. Data from quadruplet QL2.P.11.

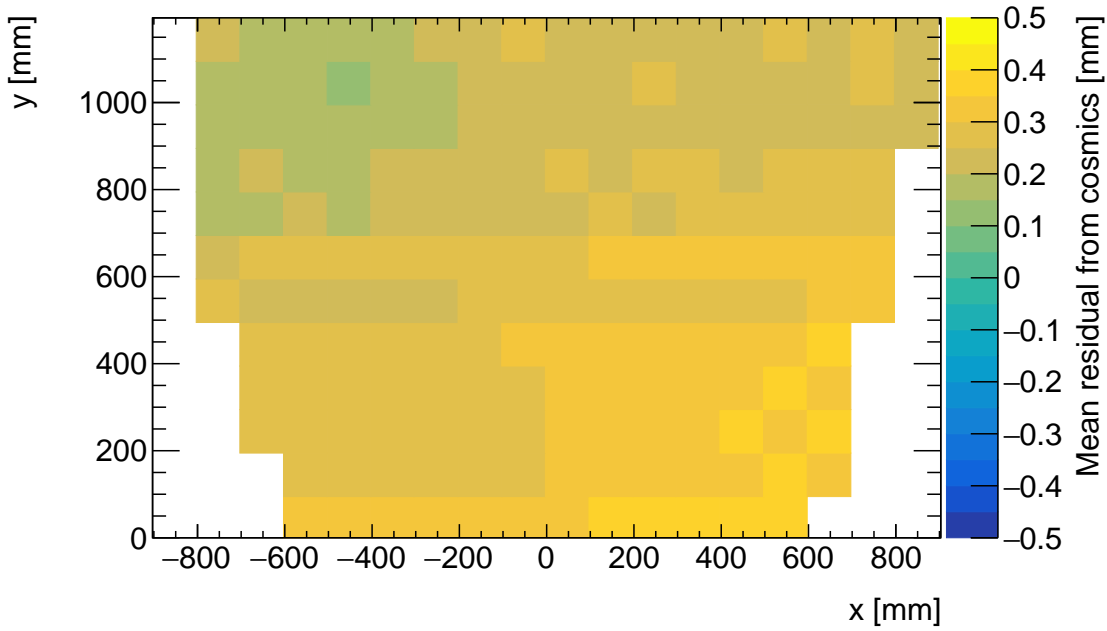
761 systematic uncertainties. The bin size of 200 μm for the distributions shown in figure 5.5 was
762 chosen based on the uncertainty on residuals calculated from tracks on layer 4 (1) built from
763 hits on layers 1 and 2 (3 and 4) given a cluster y -position uncertainty of 60 μm (appendix A.3),
764 since these tracks yield residuals with the largest uncertainties.

765 A gaussian fit was used to extract the mean of the residual distributions. Theoretically, a
766 double gaussian distribution is more apt, but for this analysis the gaussian fit was sufficient,
767 as discussed in appendix C.1.

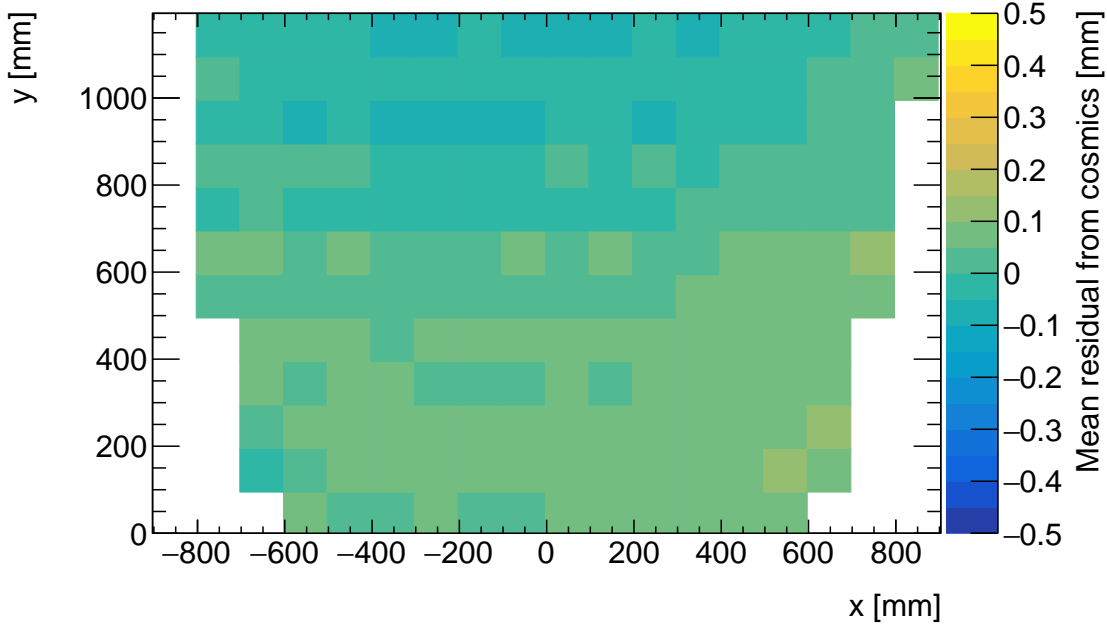
768 The area of the region of interest was 100 mm by 100 mm. The size balanced the amount of
769 tracks falling in the region of interest to give a small statistical uncertainty on the extracted
770 mean while being smaller than the order on which local offsets were expected to change
771 significantly. The change in local offsets over the surface of a layer can be modeled using
772 global alignment parameters. Using a base alignment model with a global offset and rotation
773 of each strip layer, “significantly” was defined by the distance in x that a large but possible
774 rotation of 1000 μrad would change the local offset by more than 50 μm – half the required
775 position resolution of the sTGCs [5].

776 5.6 Visualizing relative alignment between layers

777 The mean of residuals was plotted across entire strip layers for every tracking combination to
778 get a picture of the how relative local offsets change over the layers’ surface. Figure 5.6 shows
779 the mean of residuals on layer 2 with reference layers 1 and 3 for two different quadruplets,
780 referred to as QL2.P.11 and QL2.P.8, for 100 mm by 100 mm areas across the surface of
781 layer 2. To understand these plots, realize that the Gaussian mean of the distribution in
782 figure 5.5a is the entry in area bin $x \in [197, 297]$, $y \in [594.6, 694.6]$ mm in figure 5.6a.



(a) Mean of residuals of tracks on layer 2, reference layers 1 and 3, for QL2.P.11.



(b) Mean of residuals of tracks on layer 2, reference layers 1 and 3, for QL2.P.8.

Figure 5.6: Mean of residuals in each 100 mm by 100 mm bin over the area of the layer 2 cathode board. The entry in $x \in [197, 297]$, $y \in [594.6, 694.6]$ mm of figure 5.6a corresponds to the fitted Gaussian means in figures 5.5a. The mean of residuals in each area is inversely proportional to the relative local offset of layer 2 with respect to layers 1 and 3.

Many of the residual means are non-zero and change smoothly over the layer, indicating that there are relative local offsets stemming from misalignments between entire strip layers. Given that the residual mean changes with x in figure 5.6a, there is likely a rotation of layer 2 with respect to layers 1 and 3 on QL2.P.11, combined with an offset of the entire layer. The residual means are smaller in figure 5.6b indicating that QL2.P.8 is less misaligned overall than QL2.P.11; however the relative local offsets range between $\pm 200 \mu\text{m}$ so they are still significant considering the order on which the chambers must be sensitive to position, $\sim 100 \mu\text{m}$.

5.7 Systematic uncertainty

The statistical uncertainty on the local residual means was typically around $10 - 20 \mu\text{m}$, and appendix B shows that the analysis was not statistically limited by the number of triggers collected for each quadruplet. The systematic uncertainties were more significant.

Systematic uncertainties were assigned per tracking combination as the RMS of the distribution of the difference in residual means each calculated in a different way. For example, the RMS associated with fitting the local residual distributions with a Gaussian or double Gaussian is $25 \mu\text{m}$ for the geometrically least favourable tracking combinations. The distribution is shown in appendix C.1. For geometrically similar tracking combinations (like: tracks on layer 1 built from hits on layers 3 and 4, and tracks on layer 4 built from hits on layers 1 and 2), the systematic uncertainty was assigned as the average RMS of both.

Other choices were: whether to use data collected at 2.9 kV or 3.1 kV (both are collected at McGill); what cluster fitting algorithm to use; and whether or not to apply a differential non-linearity (DNL) correction to the cluster y -positions [6]. A systematic uncertainty was assigned using the method above to account for the effect of each choice and quantify the robustness of the mean of residuals. The reasons for each choice are listed below.

Data taken at 3.1 kV was used over 2.9 kV because the strip and wire tracking efficiency increases with higher voltage [58] (appendix C.2).

The Minuit2 package [65] was used to fit clusters over Guo's method [66] because it provided automatic statistical uncertainty estimates and is the standard fit algorithm of ROOT [63] (appendix C.3).

The DNL correction was not applied because its effect on the residual means was negligible (appendix C.4).

A summary of the systematic uncertainties assigned to the mean of residuals for each tracking combination is given in table 5.1.

Tracking geometry	Residual distribution fit function (C.1)	Cosmics data collection voltage (C.2)	Cluster fit algorithm (C.3)	Apply DNL correction or not (C.4)	Total
Similar to layer 3, fixed layers 1, 2	0.01	0.04	0.02	0.01	0.05
Similar to layer 4, fixed layers 1, 2	0.03	0.01	0.03	0.01	0.10
Similar to layer 2, fixed layers 1, 3	0.01	0.02	0.01	0.000	0.03
Similar to layer 4, fixed layers 1, 3	0.01	0.04	0.01	0.01	0.04
Similar to layer 2, fixed layers 1, 4	0.01	0.04	0.01	0.01	0.04

Table 5.1: Systematic uncertainty assigned for each analysis option, detailed in appendix [C](#).

816 The uncertainty in each mean of residuals was assigned as the sum in quadrature of the sta-
817 tistical uncertainty in the mean and the appropriate systematic uncertainty for the tracking
818 combination.

819 5.8 Discussion

820 Cosmics data is being used to calculate relative alignment parameters using two other meth-
821 ods [58]. The results of this analysis could be cross-checked with the other methods; however
822 the studies in appendix C show that the residual means are robust, so the comparison was
823 not prioritized.

824 Given that the uncertainty in the residual means is lesser than or near to the order of the
825 required position resolution of the sTGCs (100 μm [5]) they are relevant input for alignment
826 studies.

827 The relative local offsets as calculated from the mean of residual distributions provide a
828 complete picture of the relative alignment between detectors planes. In fact, cosmic muon
829 testing is the only characterization technique where the entire surface of quadruplet layers
830 can be probed since muons hits are distributed almost uniformly; the CMM [7] and x-ray
831 methods [8] depend on measurements at reference points, and test beams only have a limited
832 beam spot [6]. By looking at 2D-histograms of residual means like figure 5.6 for all tracking
833 combinations, it is easy to identify quadruplets that suffer large relative misalignment since
834 many residual means differ significantly from zero. Moreover, the pattern in the residual
835 means can be used to motivate a physical interpretation of misalignments. The residual
836 means can be used as a reference, cross check, or input in other alignment studies.

837 Relative local offsets cannot be used to position strips in the absolute ATLAS coordinate
838 system because there was no external reference to measure positions on all layers with re-
839 spect to. The lack of external reference means that there is not enough information to unfold
840 relative local offsets into absolute local offsets (with respect to the nominal quadruplet ge-
841 ometry). As an example, assuming that the residual on layer 2 in figure 5.4 is representative
842 of the absolute value of the relative local offset, the residual on layer 2 could be caused by
843 the strips on layer 2 being misaligned from nominal, but it could also be caused by strips
844 on layers 1 and 4 being offset from nominal while the strips on layer 2 are in their nominal
845 positions! Any number of combinations of local offsets on layers 1, 2 and 4 could produce
846 the residual on layer 2. Absolute local offsets must be calculated another way.

⁸⁴⁷ Chapter 6

⁸⁴⁸ Using x-rays to measure relative strip ⁸⁴⁹ position offsets

⁸⁵⁰ Local offset measurements were done with the x-ray method. The reader is referred to the
⁸⁵¹ paper describing the x-ray method [8], although some minor changes have been made to the
⁸⁵² experimental setup since it was written. The experimental setup described here is current
⁸⁵³ and was used to collect the data presented in this thesis.

⁸⁵⁴ 6.1 Experimental setup

⁸⁵⁵ The x-ray tests were performed after the quadruplets arrived at CERN, were assembled into
⁸⁵⁶ wedges, and alignment platforms installed. Essentially, an x-ray gun was attached to one
⁸⁵⁷ of the alignment platforms glued to the surface of the wedge and the x-ray beam profile
⁸⁵⁸ recorded by the strips.

⁸⁵⁹ The wedges were installed on carts that could rotate their surface to a horizontal position. A
⁸⁶⁰ mounting platform was installed on top of the alignment platform using a three-ball mount.
⁸⁶¹ The x-ray gun used was an [Amptek Mini-X tube](#). The gun was placed in a brass holder
⁸⁶² with built-in 2 mm collimator and 280 μm copper filter. The holder was mounted on one
⁸⁶³ of five positions on the mounting platform, as shown in figure 6.1. Gun positions were
⁸⁶⁴ chosen to avoid wire support structures in the sTGCs that reduce hit efficiency [58] and
⁸⁶⁵ boundaries between sets of strips read out by two different ASICs that could each have
⁸⁶⁶ different thresholds.

⁸⁶⁷ As with cosmics data collection, each sTGC also needed gas and high voltage to operate.

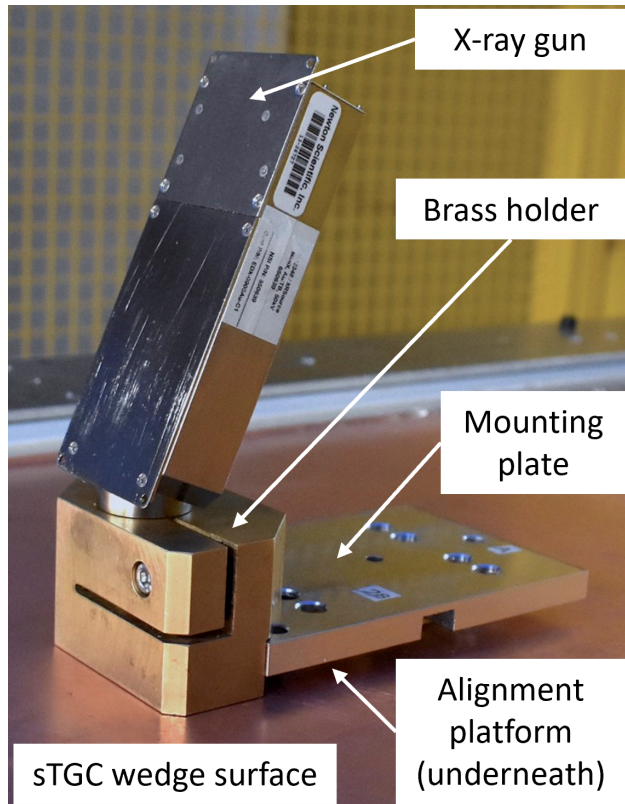


Figure 6.1: The x-ray gun mounted to the alignment platform on the surface of the wedge.
Adapted from [8].

868 Each layer was operated at 2.925 kV with high voltage from a NIM crate. The chambers
869 were flushed with CO₂ before and during data collection.
870 The gun produced x-rays with energies under 40 keV with peaks in the 7-15 keV range. Peaks
871 in the 0-30 keV range were filtered out by the copper filter and the copper of the sTGCs.
872 The x-rays mostly interacted with the wedge's copper electrodes and gold-plated tungsten
873 wires via the photo effect. The resulting photoelectrons caused ionization avalanches that
874 were picked up by the strips.

875 6.2 Data acquisition

876 A different version of the same front end electronics, but the same ASIC, as used in cosmics
877 testing were used for the x-ray testing to amplify the electrode signals and measure the peak
878 signal amplitude. Data was collected for two minutes per gun position with random triggers.
879 A trigger recorded all signals above threshold. Pad and wire data was not recorded.

880 6.3 Data preparation

881 Like with cosmics analysis, a default pedestal is subtracted from the signal peak amplitude
882 on each electrode.

883 Clusters are defined as groups of contiguous strip hits collected within 75 ns. The peak signal
884 amplitude of each electrode in a cluster is fit with a Gaussian, and the mean of the Gaussian
885 is taken as the cluster position. Cluster positions are corrected for DNL (see definition in
886 appendix C.4). Only clusters composed of hits on 3-5 strips were used in the x-ray analysis.
887 Clusters with signal on more than 5 strips were cut because they were most likely caused by
888 photoelectrons ejected with enough energy to cause more primary ionization and subsequent
889 avalanches as δ -rays.

890 The x-ray analysis diverges entirely from the cosmics analysis algorithm here because the x-
891 rays do not leave tracks. The signals picked up by the strips are from ionization avalanches [54]
892 generated by photoelectrons liberated from the metals of the sTGCs, which only travel
893 through one gas volume and are ejected at all angles. Instead of creating tracks, the cluster
894 position distribution on each layer is used to define the beam profile. A typical beam profile
895 is shown in figure 6.2.

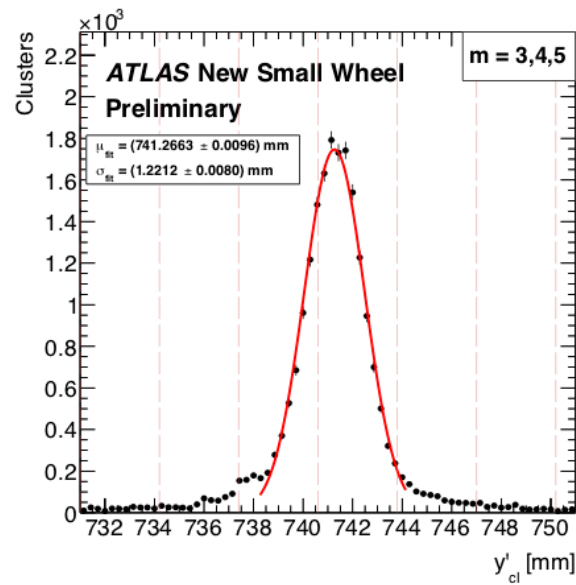


Figure 6.2: Distribution of x-ray cluster mean positions after the analysis cuts and corrections. The strip cluster multiplicity, m , was limited to 3, 4 and 5. The red curve is a Gaussian fit of the distribution and the pink dashed lines denote the edges of the strips [8].

896 **6.4 Measuring local offsets**

897 The mean of the cluster position distribution is taken as the x-ray beam profile center. The
898 expected center is calculated for each gun position using the nominal quadruplet geometry
899 parameters. The nominal position is corrected for the geometry of the brass holder and the
900 positioning and angle of the alignment platforms and the beam angle. The difference between
901 the expected and reconstructed beam profile center is a measure of the local offset. Applying
902 the logic of equation 5.1 to the beam profile, the Gaussian mean of cluster positions on the
903 given layer acts as the recorded position, y_i , the expected center is $y_{nom,i}$ and the local offset
904 is $d_{local,i}$ as before, where i denotes the layer. Since the position of the alignment platforms
905 will be monitored by the alignment system in ATLAS [5], the position of the strips that
906 should have been at the gun position are shifted by $d_{local,i}$ and so are known in the ATLAS
907 coordinate system for every position where x-ray data was taken.

908 The x-ray working group accepted an uncertainty of 120 μm on the beam profile centers. The
909 largest uncertainty comes from the effect of the gun angle, which proved difficult to measure
910 and correct for.

911 The local offsets are not presented here as the author did not conduct this work. However,
912 the author used the local offsets to calculate relative local offsets.

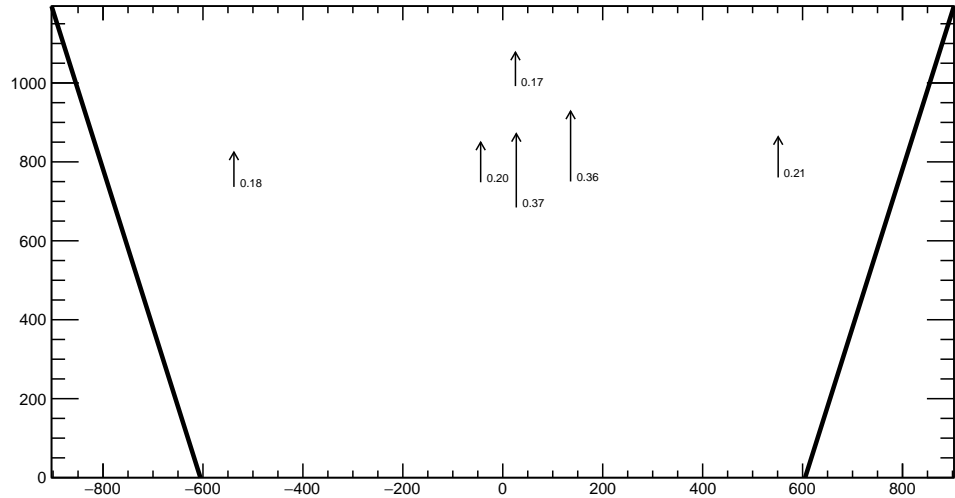
913 **6.5 Measuring relative local offsets**

914 The x-ray local offsets were shown to be correlated with the local offsets calculated from
915 the CMM data, but the CMM data does not include the effect of inter-layer misalignments
916 so the degree of correlation measurable was limited. Cosmics data is affected by inter-layer
917 misalignments. Since the local offsets for x-rays and cosmics data are measured in different
918 coordinate systems, they cannot be compared directly. Bringing the cosmics relative local
919 offsets into an absolute coordinate system is impossible; however, the x-ray local offsets can
920 be brought into a relative coordinate system.

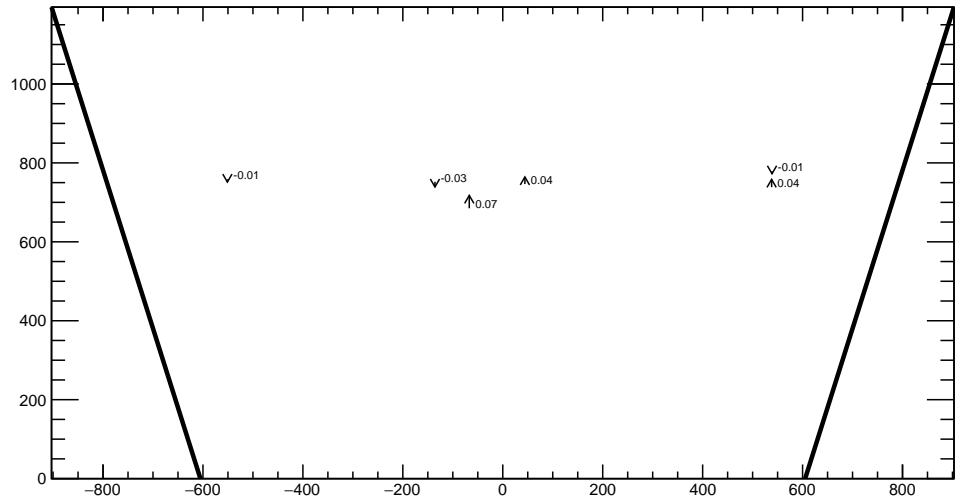
921 The measured x-ray beam profile centers were systematically affected by local offsets in the
922 same way as the mean cosmics residuals, as modeled by equation 5.1. Therefore, if a 2-layer
923 track is built from the beam profile centers on each layer and the residual calculated on a
924 third layer, that residual should match the local mean cosmics residual. The residual is the
925 difference between the beam profile center on the layer of interest and the polated track
926 position from the beam profile centers recorded on the two fixed layers. The beam profile
927 center on the layer of interest acts as y_i and the polated track position acts as $y_{track,i}$ in
928 equation 5.2.

929 The track referred to here is not an actual track of the x-ray beam. A beam profile center
930 is actually the Gaussian mean of all selected mean cluster positions recorded during the
931 x-ray data taking period, not a single hit of a track. Building an “abstract” track was
932 necessary because the x-rays cause signal in the chamber via the photoeffect so there were
933 not individual “x-ray tracks” to record. In fact the x-ray data could be collected separately
934 for each layer. Nonetheless, since the effect of local offsets on the beam profile centers was
935 the same as their effect on the cosmics cluster positions the difference in algorithm between
936 x-ray and cosmics analysis was allowed.

937 For each x-ray survey position, the x-ray residual was calculated for all possible tracking
938 combinations (which required an x-ray beam profile on at least three layers). The x-ray
939 residuals on layer 2 calculated from the beam profile centers recorded on layers 1 and 3 are
940 represented as arrows for QL2.P.11 and QL2.P.8 in figure 6.3. For QL2.P.11, a negative
941 relative local offset at all x-ray survey positions is clear.



(a) QL2.P.11 x-ray residuals on layer 2, reference layers 1 and 3.



(b) QL2.P.8 x-ray residuals on layer 2, reference layers 1 and 3.

Figure 6.3: The x-ray residuals on layer 2 calculated from the beam profile centers recorded on layers 1 and 3 for QL2.P.11 and QL2.P.8. The arrows originate from the expected position of the beam profile center assuming a nominal geometry, and the lengths are proportional to the calculated x-ray residuals. The value of the x-ray residuals are annotated in millimeters and have an uncertainty of ± 0.15 mm.

942 The uncertainty on the x-ray residuals was the error propagated through the tracking, taking
943 an uncertainty of 120 μm on each beam profile center. The uncertainty on the x-ray residuals
944 ranged from 0.15 mm to 0.4 mm from the most to least geometrically-favourable tracking
945 combination. There is no discernible pattern to the x-ray residuals on QL2.P.8 because they
946 have absolute values smaller than the uncertainty on the x-ray residuals. The x-ray residual
947 uncertainties are significantly larger than the uncertainties on the mean cosmics residuals.

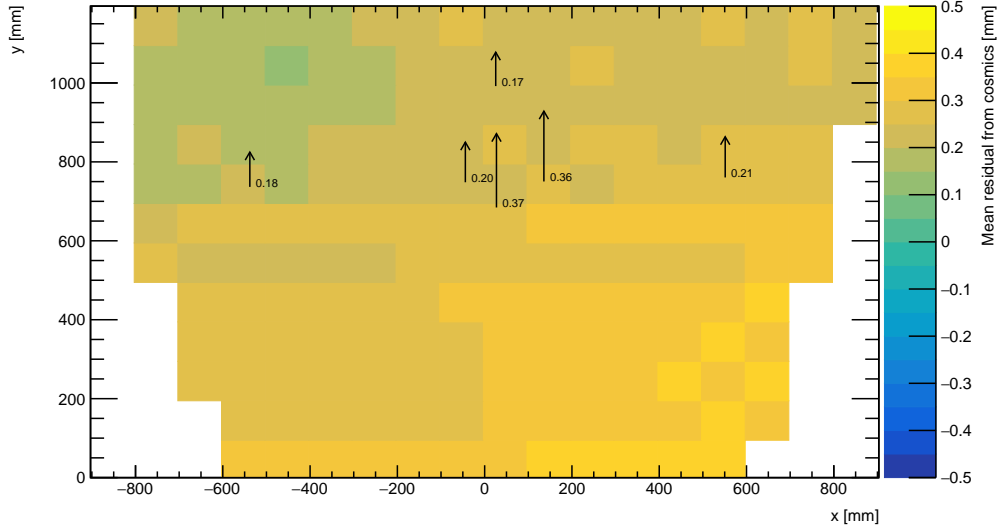
948 **Chapter 7**

949 **Comparing cosmic muon and x-ray
950 relative strip position offsets**

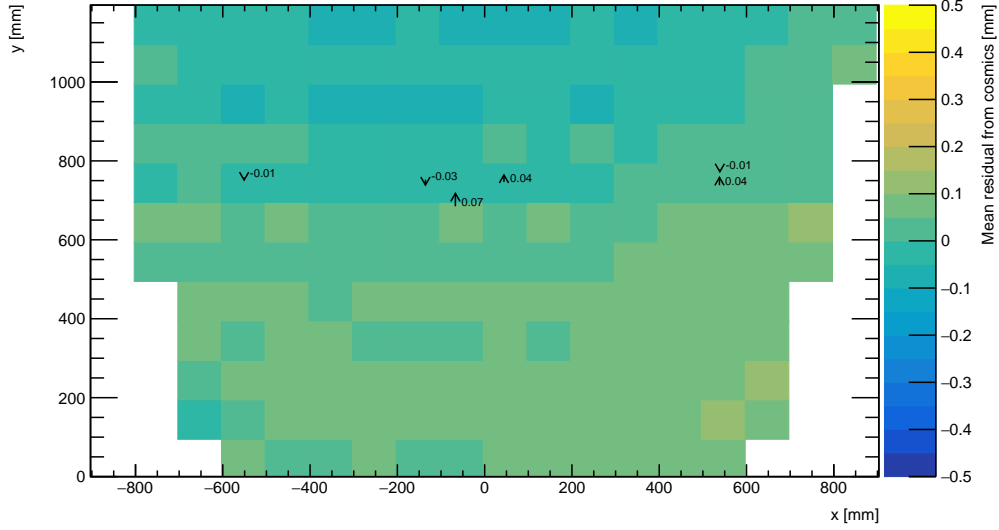
951 The goal was to validate the local offsets extracted from the x-ray data with cosmics data.
952 The complication was that the x-ray dataset provided absolute local offsets while the cosmics
953 dataset provided relative local offsets, which could not be compared directly. The solution
954 was to use the x-ray local offsets to calculate relative local offsets. The x-ray relative local
955 offset is opposite sign to the x-ray residual reconstructed from an abstract track using the
956 beam profile centers on each layer as the track hits. The cosmics relative local offset was
957 inferred from the Gaussian mean of muon track residuals in a 100 mm by 100 mm area,
958 referred to the as the mean cosmics residual. Residuals of each type calculated using the
959 same reference layers are compared for each area where x-ray data is available. The results
960 of the comparison are presented here.

961 **7.1 Assessing correlation**

962 The 2D visualizations of the mean cosmics and x-ray residuals for tracks on layer 2 with
963 reference layers 1 and 3 on QL2.P.11 and QL2.P.8 are shown in figure 7.1. Figure 7.1 is a
964 superposition of figures 5.6 and 6.3.



(a) QL2.P.11 residuals of tracks on layer 2, reference layers 1 and 3.



(b) QL2.P.8 residuals of tracks on layer 2, reference layers 1 and 3.

Figure 7.1: The mean cosmics residuals are shown using colour. The x-ray residuals available at nominal gun positions are drawn as arrows and the value of the residual annotated in millimeters with uncertainty ± 0.15 mm. The length of the arrows is 500 times the value of the x-ray residual, scaled for visibility. These plots are a superposition of figures 5.6 and 6.3.

965 Figure 7.1a shows that for QL2.P.11 the x-ray residuals are of the same sign and order as the
966 mean cosmics residuals, as can be seen by comparing the the annotated value of the x-ray
967 residual to the mean cosmics residual represented by colour; QL2.P.11's mean cosmics and x-
968 ray residuals are correlated to some degree. For QL2.P.8, the x-ray residuals are of the right
969 order compared to the mean cosmics residuals, but the correlation is not apparent. While
970 x-ray residuals do not reveal a pattern in relative local offset across the layer's surface, the
971 mean cosmics residuals show a structure to the relative local offsets since they vary smoothly
972 over the surface of layer 2.

973 The comparison of mean cosmics and x-ray residuals was done for several quadruplets for all
974 tracking combinations (not just layer 2 residuals calculated with fixed layers 1 and 3 like in
975 figure 7.1). Scatter plots of the x-ray and mean cosmics residuals on QL2.P.11 and QL2.P.8
976 for all tracking combinations shown in figures 7.2 and 7.3 reveal the degree of correlation
977 between the datasets. In the correlation plots, each rectangle is centered on the value of a
978 mean cosmics and x-ray residual pair calculated with a given tracking combination for every
979 gun position where data is available; the height and width of the squares are the uncertainty
980 in the mean cosmics and x-ray residuals respectively. Note that in the scatter plots, the
981 regions of interest where cosmics tracks are included in the calculation of mean of residuals
982 are exactly centered on the nominal x-ray beam position, unlike in figure 7.1.

983 The fitted slope and offset in figure 7.2 show that the two QL2.P.11 datasets are correlated.
984 The large uncertainty on the x-ray residuals set a limit on the sensitivity of the analysis,
985 for if the absolute value of the x-ray residuals of a quadruplet were smaller than the x-ray
986 residual uncertainties, no conclusion about the correlation could be drawn, like for QL2.P.8
987 (figure 7.3). This result is reflected in the small x-ray residuals shown in figure 7.1b that
988 do not reveal a pattern in the relative local offsets across the surface of layer 2. However,
989 figure 7.3 shows that the x-ray and mean cosmics residuals are clustered around zero, as is
990 expected for a quadruplet with small relative misalignments between layers.

991 There are three patterns in the residuals on the scatter plot explained by geometry. First,
992 for both datasets the uncertainty in the extrapolated track residuals were larger than the
993 interpolated track residuals because of the extrapolation lever arm. For the x-ray residuals,
994 the effect of the lever arm on the uncertainty was direct since the residual was calculated from
995 a single abstract track; for the mean cosmics residuals it was the widening of the residual
996 distribution due to the extrapolation lever arm that increased the uncertainty in the fitted
997 mean of residuals. Second, residuals calculated through extrapolation tend to be larger
998 because the extrapolation lever arm can produce more extreme values of the track position
999 on the layer of interest. Third, the points in figure 7.2 are geometrically correlated (e.g.
1000 they seem to be roughly mirrored around the origin). This is expected since the residuals
1001 calculated using a given set of three layers should be geometrically correlated by the local

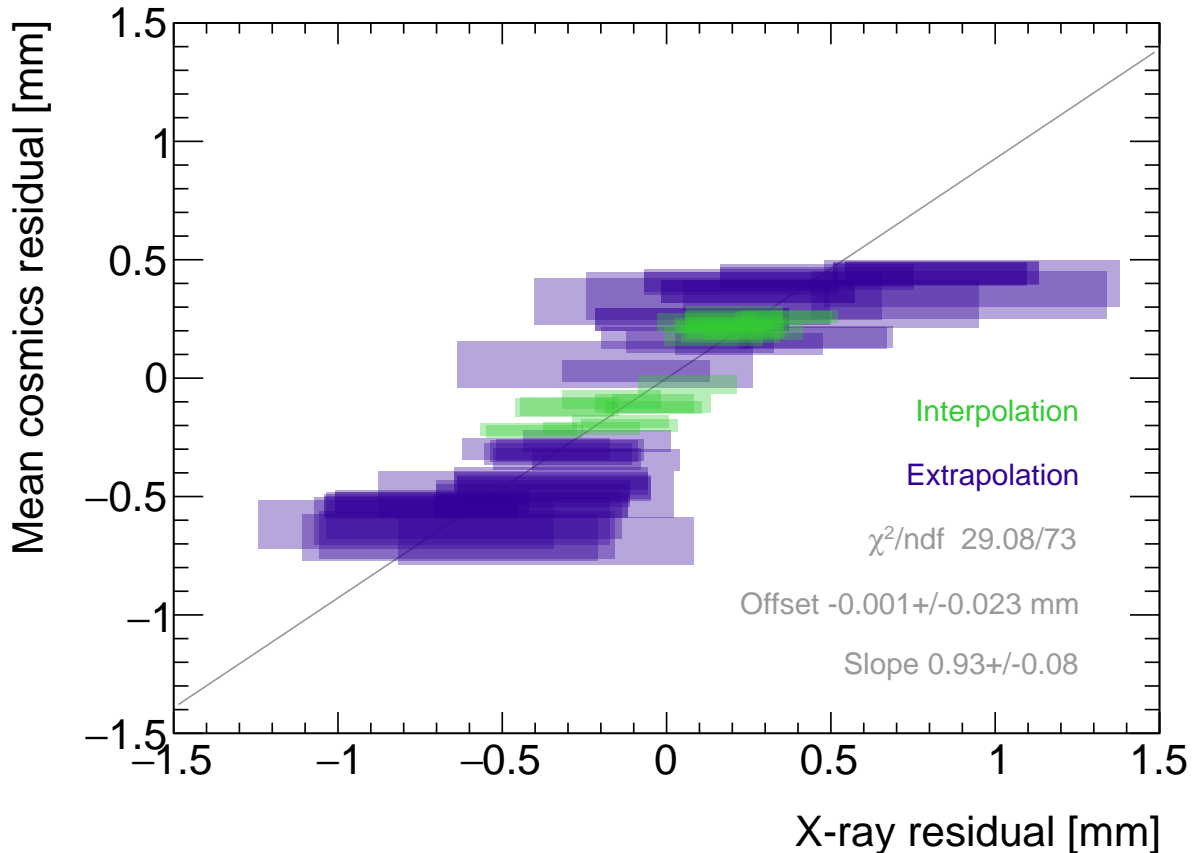


Figure 7.2: Correlation plot between x-ray and mean cosmics residuals for all tracking combinations for QL2.P.11. Each rectangle is centered on an x-ray and mean cosmics residual pair calculated at a given gun position and for a certain tracking combination. The width of the rectangles in x and y are the uncertainty in the x-ray and mean cosmics residual respectively. A printer-friendly version of this plot is available in appendix D.

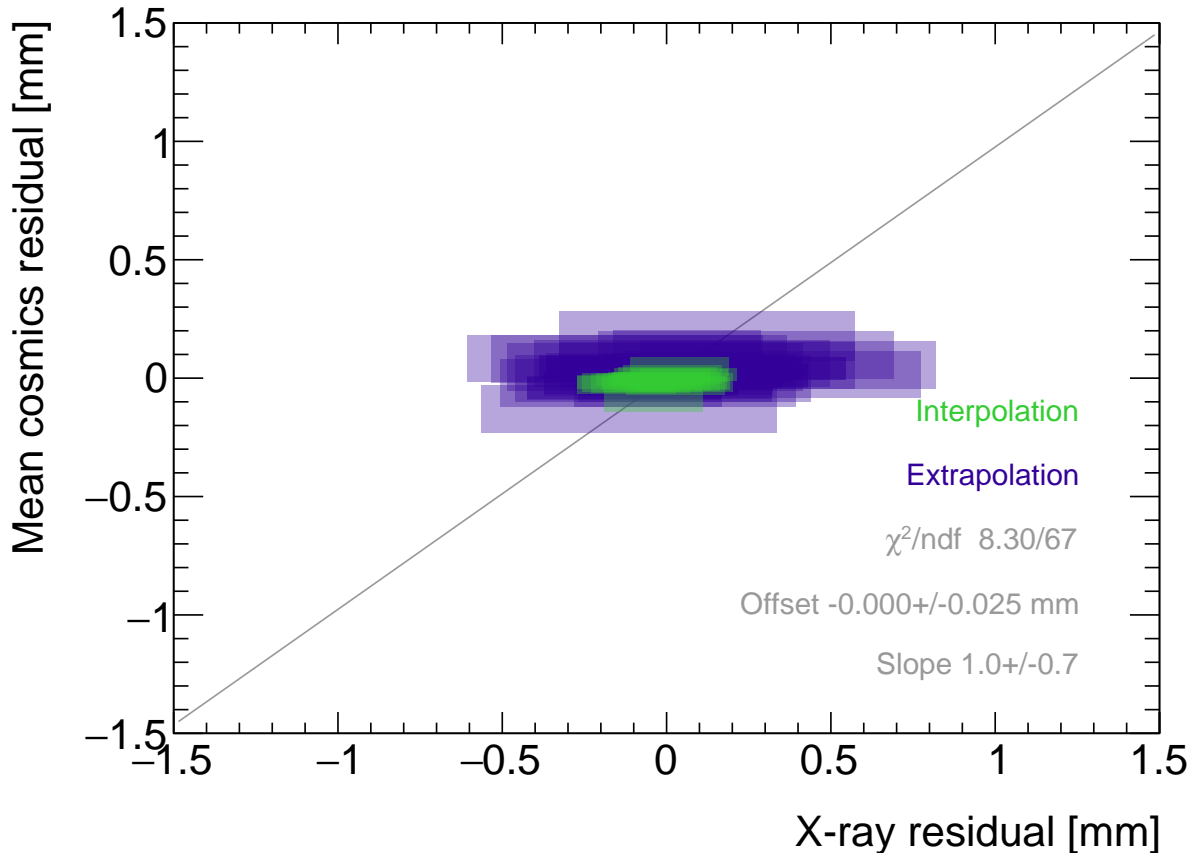


Figure 7.3: Correlation plot between x-ray and mean cosmics residuals for all tracking combinations for quadruplet 2. Each rectangle is centered on an x-ray and mean cosmics residual pair calculated at a given gun position and for a certain tracking combination. The width of the rectangles in x and y are the uncertainty in the x-ray and mean cosmics residual respectively. A printer-friendly version of this plot is available in appendix D.

1002 offsets on each layer (the $d_{local,i}$ on each layer as defined in equation 5.1).

1003 7.2 Discussion

1004 Several quadruplets were tested for each quadruplet construction geometry built in Canada.
1005 Each quadruplet fell into one of the two categories: residuals large enough to see a correlation,
1006 or residuals too small to see a correlation. Since the x-ray and mean cosmics residuals can
1007 be used to calculate relative local offsets between the layer and the two reference layers,
1008 quadruplets with the largest relative misalignments had the largest range of residuals. The
1009 correlation plots are another easy visual way to identify quadruplets with large relative
1010 misalignments.

1011 The most significant limit on measuring the degree of correlation between the x-ray and
1012 mean cosmics residuals was the uncertainty on the x-ray residuals, which stemmed from the
1013 systematic uncertainty of 120 μm in the x-ray beam profile centers used to build the abstract
1014 tracks. For example, in figure 7.3, if the x-ray residuals could be known to within better
1015 precision, perhaps they would be correlated with the mean cosmics residuals. The x-ray
1016 method was limited primarily by the systematic uncertainties in the relative alignment of
1017 the platforms and the gun, especially the gun angle.

1018 The analysis of certain quadruplets was limited by the availability of data. Sometimes,
1019 less than three layers were surveyed for a given x-ray gun position so no residuals could
1020 be calculated. Too few x-ray residuals prevented the analysis from detecting a significant
1021 correlation, should it even be measurable. Often, the analysis of smaller quadruplets (placed
1022 innermost on the wheel) suffered as a result because they had fewer alignment platforms, and
1023 hence gun positions, on their surfaces. The analysis was also limited to certain quadruplets.
1024 The wedges constructed the earliest (typically small wedges) were surveyed when the x-ray
1025 method was still being designed and so have limited x-ray residuals calculated from beam
1026 profiles of lower quality. In addition, not all cosmic muon test sites had enough front end
1027 electronics to collect data on three layers simultaneously, which is the minimum required to
1028 be able to calculate residuals.

1029 Nonetheless, the comparison of x-ray and cosmics residuals was really to confirm the x-ray
1030 method's ability to measure local offsets with an independent dataset. The x-ray local offsets
1031 allow the calculation of relative local offsets that have been correlated to the cosmics relative
1032 local offsets. Therefore, the analysis of quadruplets with relative local offsets large enough
1033 to detect a correlation validates the x-ray method's ability to measure local offsets.

1034 The potential of using relative local offsets calculated from cosmics data to study relative
1035 alignment between sTGC layers stands on its own. For example, although the x-ray residuals

1036 in QL2.P.8 in figure 7.1b do not reveal a pattern, the variation in the mean cosmics residuals
1037 do. Identifying the pattern is possible because mean cosmics residuals can be calculated
1038 across the entire area and are sensitive to smaller relative local offsets since their uncertainty
1039 is significantly smaller.

1040 The advantage of the x-ray dataset over the cosmics dataset is that absolute local offsets
1041 are measurable thanks to the reference frame provided by the alignment platforms. This is
1042 required to measure the position of strips in the ATLAS coordinate system and to satisfy the
1043 NSWs' precision tracking goals. The x-ray local offsets are being used to build an alignment
1044 model of strips in each quadruplet. It is compelling to imagine using the cosmics relative
1045 local offsets to improve the model considering their precision and ability to capture effects
1046 across the entire area of the quadruplet.

1047 **Chapter 8**

1048 **Outlook and summary**

1049 The cosmic muon dataset was used to independently confirm the local offsets measured by
1050 the x-ray method. The x-ray offsets are being used to complete the sTGC alignment scheme
1051 of the NSWs: the NSW alignment system monitors the position of alignment platforms
1052 on the surface of sTGC wedges, and the x-ray measurements provide the offsets of the strip
1053 pattern with respect to each alignment platform. The continuation of this analysis is detailed
1054 next (section 8.1) before summarizing and considering the larger context (section 8.2).

1055 **8.1 Outlook**

1056 Next all quadruplets with suitable cosmics and x-ray data should be surveyed to flag anomalous
1057 quadruplets (as a first step). If a quadruplet's correlation plot like figure 7.2 or 7.3
1058 reveals an unexpected correlation or has a large scatter, it would indicate an issue with either
1059 the cosmics or x-ray data collection to be investigated further. The uncertainty in each
1060 set of tracking points would inform the interpretation of the anomaly. Then, the quality of
1061 the correlation should be evaluated over all quadruplets instead of individually.

1062 For now, the correlation of the individual quadruplets tested support the use of the x-ray
1063 data to build an alignment model [8]. Work on creating an alignment model is ongoing.
1064 Currently, the algorithm compares the offsets of a local group of strips at each x-ray gun
1065 position as measured by the x-ray and CMM methods in a fit to extract a global slope (m)
1066 and offset (b) per layer, i , where the χ^2 is given by equation 8.1.

$$\chi^2 = \frac{[dy_{cmm,corr} - dy_{xray}]^2}{\delta dy_{xray}^2 + \delta dy_{cmm,corr}^2}, \quad (8.1)$$

1067

$$dy_{cmm,corr} = y_{cmm} + b_i + m_i x - y_{nom} \quad (8.2)$$

1068 Here, dy is an offset as calculated from the x-ray and corrected CMM data and δdy refers
 1069 to their respective uncertainties. The CMM measurements were taken before the cathode
 1070 boards were assembled into quadruplets, so alignment parameters for the given layer were
 1071 extracted from the χ^2 fit by stepping the corrected CMM y -position towards the x-ray y -
 1072 position by adjusting the layer's slope and offset parameters. The plan is that the alignment
 1073 parameters will be provided to the ATLAS experiment's offline software to reconstruct muon
 1074 tracks from the NSWs' sTGCs. The large uncertainty on the x-ray local offsets (120 μm) and
 1075 the sparseness of the measurements means that including input from other characterization
 1076 datasets could reduce the uncertainty on the alignment model parameters.

1077 The uncertainty in the mean cosmics residuals was smaller than the desired position reso-
 1078 lution of the sTGCs, so they provide relevant information about strip positions. Moreover,
 1079 they can be calculated over the entire area of the quadruplet instead of at specific posi-
 1080 tions. It would be great to use the cosmics residuals as input to calculate and reduce the
 1081 uncertainty on the alignment parameters. Since mean cosmics residuals can only provide
 1082 relative alignment information, one idea would be to use them to constrain the fit of the
 1083 alignment parameters. In this case, the alignment parameters would need to be fitted on all
 1084 layers at once, and the shifting y -positions on each layer forced to create an abstracted track
 1085 residual equal to the local mean cosmics residual (within uncertainty) for each x-ray point.
 1086 Or, instead of constraining the fit, it could be penalized if the resulting parameters do not
 1087 result in abstracted track residuals equal to the mean cosmics residuals within uncertainty.
 1088 Some work on using the three datasets at once in a fit has been started.

1089 8.2 Summary

1090 The LHC [1] will be at the energy frontier of particle physics for at least the next decade,
 1091 making it a unique tool with which to study particle physics. With the HL-LHC [2], high
 1092 statistics on rare particle physics processes will enable more precise measurements of param-
 1093 eters of the Standard Model and increase the sensitivity to signatures of physics beyond the
 1094 Standard Model [3]. To capitalize on the increased collision rate, the NSWs of the ATLAS
 1095 experiment must be replaced to keep the triggering and tracking performance [5].
 1096 Small-strip thin gap chambers are gas ionization chambers optimized for a high rate envi-
 1097 ronment [5]. Using the pad electrodes to define a region of interest makes it possible to get
 1098 track segments of ~ 1 mrad angular resolution quickly, which will be used as input to check

1099 if a collision originated from the interaction point and should be triggered on or not [5, 53].
1100 sTGCs are also able to provide better than 100 μm position resolution on each detector plane
1101 to fulfill precision offline tracking requirements [6].

1102 Ultimately, the positions of the sTGC strip electrodes need to be known in ATLAS to within
1103 $\sim 100 \mu\text{m}$ so that they can deliver the required position resolution. The ATLAS alignment
1104 system will position alignment platforms on the surface of the sTGC wedge, and an alignment
1105 model will be used to position the strips with respect to the alignment platforms [5]. Input
1106 to the alignment model comes from the datasets used to characterize the quadruplets. The
1107 x-ray method [8] is used to measure offsets of strips from their nominal position to achieve
1108 this goal. The alignment model could be built on x-ray data alone, but the sparseness of
1109 and large uncertainty on the local offsets mean that the alignment model could benefit from
1110 more input. Comparing the x-ray offsets to the CMM data [7] allows the effect of inter-layer
1111 misalignments to be isolated and increases the input to the alignment model.

1112 The cosmics dataset was used to confirm the local offsets measured with the x-ray gun. It
1113 provides relative local offsets between sTGC strip layers. The 2D visualizations of relative
1114 local offsets allow personnel to quickly identify areas of misaligned strips and make hypothe-
1115 ses of the physical origin of those misalignments. The correlation seen between the x-ray and
1116 cosmics residuals in quadruplets with large relative misalignments confirms the validity of
1117 the x-ray local offsets. Moreover, the mean of track residuals in an area can be used to make
1118 a robust estimation of the relative local offset, as shown by the estimation of systematic
1119 uncertainties; the relative local offsets for all two-fixed layer reference frames do not change
1120 by more than 100 μm given variation in data collection conditions and analysis algorithms.
1121 The cosmics relative local offsets are therefore relevant input for alignment studies and could
1122 improve the alignment model that will position each strip.

1123 Achieving the required position resolution on each layer of the NSWs in the particle track
1124 bending plane achieves the design momentum resolution for muons ejected towards the end-
1125 caps of ATLAS. Muons are important signatures of electroweak and Higgs sector events
1126 of interest for the ATLAS Collaboration’s future physics goals [5]. Being the second of two
1127 tracking technologies on the NSWs, an effective alignment model of sTGC quadruplets layers
1128 is a necessary part of making the NSWs redundant for 10 or more years of recording collisions
1129 in the High Luminosity era of the LHC.

1130 References

- 1131 [1] L. Evans and P. Bryant. LHC Machine. *Journal of Instrumentation*, 3(S08001), August
1132 2008.
- 1133 [2] G. Apollinari et al. High-Luminosity Large Hadron Collider (HL-LHC) Technical Design
1134 Report V. 0.1. Technical Report CERN-2017-007-M, CERN, Geneva, September 2017.
- 1135 [3] A. Dainese et al. The physics potential of HL-LHC. In *Input to the European Particle
1136 Physics Strategy Update*, November 2018.
- 1137 [4] The ATLAS Collaboration. The ATLAS Experiment at the CERN Large Hadron Col-
1138 linder. *Journal of Instrumentation*, 3(08):S08003, August 2008.
- 1139 [5] T. Kawamoto et al. New Small Wheel Technical Design Report. Technical Report
1140 CERN-LHCC-2013-006, ATLAS-TDR-020, CERN, Geneva, June 2013.
- 1141 [6] A. Abusleme et al. Performance of a Full-Size Small-Strip Thin Gap Chamber Prototype
1142 for the ATLAS New Small Wheel Muon Upgrade. *Nuclear Instruments and Methods in
1143 Physics Research Section A: Accelerators, Spectrometers, Detectors and Associated
1144 Equipment*, 817:85–92, May 2016. arXiv: 1509.06329.
- 1145 [7] E.M. Carlson. *Results of the 2018 ATLAS sTGC test beam and internal strip alignment
1146 of sTGC detectors*. M.Sc. thesis, University of Victoria, Victoria, Canada, 2019.
- 1147 [8] B. Lefebvre. Precision survey of the readout strips of small-strip Thin Gap Chambers
1148 using X-rays for the muon spectrometer upgrade of the ATLAS experiment. *Journal of
1149 Instrumentation*, 15(07):C07013–C07013, July 2020.
- 1150 [9] D.J. Griffiths. *Introduction to elementary particles*. Physics textbook. Wiley-VCH,
1151 Weinheim, Germany, 2., rev. ed., 5. reprint edition, 2011.
- 1152 [10] M.E. Peskin and D.V. Schroeder. *An introduction to quantum field theory*. Addison-
1153 Wesley Pub. Co, Reading, Massachusetts, 1995.

- 1154 [11] P.A. Zyla et al. Review of Particle Physics. *PTEP*, 2020(8):083C01, 2020.
- 1155 [12] M. Kobayashi and T. Maskawa. CP-violation in the renormalizable theory of weak
1156 interaction. *Progress of theoretical physics*, 49(2):652–657, February 1973.
- 1157 [13] M.L. Perl et al. Evidence for Anomalous Lepton Production in $\{e\}^{\{+}\backslash ensuremath{-}\} \{e\}^{\{\backslash ensuremath{-}\}}\$$ Annihilation. *Physical Review Letters*, 35(22):1489–1492, De-
1158 cember 1975. Publisher: American Physical Society.
- 1160 [14] F. Englert and R. Brout. Broken Symmetry and the Mass of Gauge Vector Mesons.
1161 *Physical Review Letters*, 13(9):321–323, August 1964. Publisher: American Physical
1162 Society.
- 1163 [15] P.W. Higgs. Broken symmetries, massless particles and gauge fields. *Physics Letters*,
1164 12(2):132–133, September 1964.
- 1165 [16] D. Galbraith and C. Burgard. UX: Standard Model of the Stan-
1166 dard Model, November 2013. [http://davidgalbraith.org/portfolio/
1167 ux-standard-model-of-the-standard-model/](http://davidgalbraith.org/portfolio/ux-standard-model-of-the-standard-model/) last accessed on 2021-09-30.
- 1168 [17] C.A. Bertulani. *Nuclear physics in a nutshell*. In a nutshell. Princeton University Press,
1169 Princeton, N.J, 2007. OCLC: ocm85690422.
- 1170 [18] B.W. Carroll and D.A. Ostlie. *An introduction to modern astrophysics*. Pearson
1171 Addison-Wesley, San Francisco, 2nd ed edition, 2007. OCLC: ocm69020924.
- 1172 [19] M. Boezio and E. Mocchiutti. Chemical composition of galactic cosmic rays with space
1173 experiments. *Astroparticle Physics*, 39-40:95–108, December 2012.
- 1174 [20] The SNO Collaboration. Combined analysis of all three phases of solar neutrino data
1175 from the sudbury neutrino observatory. *Phys. Rev. C*, 88:025501, August 2013.
- 1176 [21] B. Pontecorvo. Neutrino Experiments and the Problem of Conservation of Leptonic
1177 Charge. *Soviet Physics—JETP*, 53:1717–1725, 1967.
- 1178 [22] S.M. Bilenky and S.T. Petcov. Massive neutrinos and neutrino oscillations. *Reviews of
1179 Modern Physics*, 59(3):671–754, July 1987.
- 1180 [23] B. Young. A survey of dark matter and related topics in cosmology. *Frontiers of Physics*,
1181 12(2):121201, April 2017.
- 1182 [24] C. Muñoz. Dark matter detection in the light of recent experimental results. *International
1183 Journal of Modern Physics A*, 19(19):3093–3169, July 2004.

- 1184 [25] G. Arnison et al. Experimental observation of isolated large transverse energy elec-
 1185 trons with associated missing energy at s=540 GeV. *Physics Letters B*, 122(1):103–116,
 1186 February 1983.
- 1187 [26] M. Banner et al. Observation of single isolated electrons of high transverse momentum
 1188 in events with missing transverse energy at the CERN pp collider. *Physics Letters B*,
 1189 122(5):476–485, March 1983.
- 1190 [27] G. Arnison et al. Experimental observation of lepton pairs of invariant mass around 95
 1191 GeV/c² at the CERN SPS collider. *Physics Letters B*, 126(5):398–410, July 1983.
- 1192 [28] P. Bagnaia et al. Evidence for Z → e⁺e⁻ at the CERN pp collider. *Physics Letters B*,
 1193 129(1):130–140, 1983.
- 1194 [29] The CDF Collaboration. Observation of Top Quark Production in $\bar{p}p$ Collisions with
 1195 the Collider Detector at Fermilab. *Physical Review Letters*, 74(14):2626–2631, April
 1196 1995. Publisher: American Physical Society.
- 1197 [30] The D0 Collaboration. Observation of the Top Quark. *Physical Review Letters*,
 1198 74(14):2632–2637, April 1995. Publisher: American Physical Society.
- 1199 [31] The ATLAS Collaboration. Observation of a new particle in the search for the Standard
 1200 Model Higgs boson with the ATLAS detector at the LHC. *Physics Letters B*, 716(1):1–
 1201 29, September 2012. arXiv: 1207.7214.
- 1202 [32] The CMS Collaboration. Observation of a new boson at a mass of 125 GeV with the
 1203 CMS experiment at the LHC. *Physics Letters B*, 716(1):30–61, September 2012. arXiv:
 1204 1207.7235.
- 1205 [33] Standard Model Summary Plots June 2021, June 2021. <https://atlas.web.cern.ch/Atlas/GROUPS/PHYSICS/PUBNOTES/ATL-PHYS-PUB-2021-032/> last accessed on 2021-
 1206 09-30.
- 1208 [34] O.S. Brüning et al. *LHC Design Report*. CERN Yellow Reports: Monographs. Geneva,
 1209 2004.
- 1210 [35] ATLAS luminosity public results run-1, March 2011. <https://twiki.cern.ch/twiki/bin/view/AtlasPublic/LuminosityPublicResults> last accessed on 2021-09-20.
- 1212 [36] ATLAS luminosity public results run-2, July 2015. <https://twiki.cern.ch/twiki/bin/view/AtlasPublic/LuminosityPublicResultsRun2> last accessed on 2021-09-20.

- 1214 [37] The European Strategy for Particle Physics. Technical Report CERN/2685, CERN,
1215 2006. Adopted by the CERN council at a special session at ministerial level in Lisbon
1216 in 2006.
- 1217 [38] HiLumi HL-LHC Project. LHC/HL-LHC plan (last update january 2021). <https://hilumilhc.web.cern.ch/content/hl-lhc-project>, last accessed on 2021-09-09.
- 1219 [39] M. Cepeda et al. Report from Working Group 2: Higgs Physics at the HL-LHC and
1220 HE-LHC. *CERN Yellow Reports Monographs*, 7:221–584. 364 p, Dec 2018.
- 1221 [40] ATLAS inner detector : Technical Design Report, 1. Technical Report CERN-LHCC-
1222 97-016, CERN, April 1997. ISBN: 9789290831020 Publication Title: CERN Document
1223 Server.
- 1224 [41] S. Haywood, L. Rossi, R. Nickerson, and A. Romanouk. ATLAS inner detector :
1225 Technical Design Report, 2. Technical Report CERN-LHCC-97-017, CERN, April 1997.
1226 ISBN: 9789290831037 Publication Title: CERN Document Server.
- 1227 [42] C. Grupen, B.A. Shwartz, and H. Spieler. *Particle detectors*. Cambridge University
1228 Press, Cambridge, UK; New York, 2008. OCLC: 1105536566.
- 1229 [43] ATLAS liquid-argon calorimeter : Technical Design Report. Technical Report CERN-
1230 LHCC-96-041, CERN, 1996. ISBN: 9789290830900 Publication Title: CERN Document
1231 Server.
- 1232 [44] ATLAS tile calorimeter : Technical Design Report. Technical Report CERN-LHCC-96-
1233 042, CERN, 1996. ISBN: 9789290830917 Publication Title: CERN Document Server.
- 1234 [45] The ATLAS Collaboration. ATLAS Muon Spectrometer: Technical Design Report.
1235 Technical Report CERN-LHCC-97-022, CERN, Geneva, 1997.
- 1236 [46] ATLAS magnet system : Technical Design Report, 1. Technical Report CERN-LHCC-
1237 97-018, CERN, April 1997. ISBN: 9789290831044 Publication Title: CERN Document
1238 Server.
- 1239 [47] The ATLAS Collaboration. Performance of the ATLAS muon trigger in pp collisions
1240 at $\sqrt{s} = 8$ TeV. *The European Physical Journal C*, 75(3):120, March 2015. arXiv:
1241 1408.3179.
- 1242 [48] S. Aefsky et al. The Optical Alignment System of the ATLAS Muon Spectrometer End-
1243 caps. *Journal of Instrumentation*, 3(11):P11005–P11005, November 2008. Publisher:
1244 IOP Publishing.

- 1245 [49] ATLAS level-1 trigger : Technical Design Report. Technical Report CERN-LHCC-98-
1246 014, CERN, August 1998. ISBN: 9789290831280 Publication Title: CERN Document
1247 Server.
- 1248 [50] A. Ruiz Martínez. The run-2 ATLAS trigger system. *Journal of Physics: Conference
1249 Series*, 762:012003, October 2016.
- 1250 [51] Technical Design Report for the Phase-II Upgrade of the ATLAS TDAQ System. Tech-
1251 nical Report CERN-LHCC-2017-020, ATLAS-TDR-029, CERN, Geneva, September
1252 2017.
- 1253 [52] P. Jenni, M. Nessi, M. Nordberg, and K. Smith. ATLAS high-level trigger, data-
1254 acquisition and controls : Technical Design Report. Technical Report CERN-LHCC-
1255 2003-022, CERN, July 2003.
- 1256 [53] E. Perez Codina. Small-strip Thin Gap Chambers for the muon spectrometer upgrade of
1257 the ATLAS experiment. *Nuclear Instruments and Methods in Physics Research Section
1258 A: Accelerators, Spectrometers, Detectors and Associated Equipment*, 824:559–561, July
1259 2016.
- 1260 [54] J. Townsend. *Electricity in gases*. Clarendon Press, Oxford, 1915.
- 1261 [55] S. Majewski, G. Charpak, A. Breskin, and G. Mikenberg. A thin multiwire chamber
1262 operating in the high multiplication mode. *Nuclear Instruments and Methods*, 217:265–
1263 271, 1983.
- 1264 [56] E. Gatti, A. Longoni, H. Okuno, and P. Semenza. Optimum geometry for strip cathodes
1265 or grids in MWPC for avalanche localization along the anode wires. *Nuclear Instruments
1266 and Methods*, 163(1):83–92, July 1979.
- 1267 [57] G. Battistoni et al. Resistive cathode transparency. *Nuclear Instruments and Methods
1268 in Physics Research*, 202(3):459–464, November 1982.
- 1269 [58] B. Lefebvre. *Characterization studies of small-strip Thin Gap Chambers for the ATLAS
1270 Upgrade*. PhD thesis, McGill University, Montreal, Canada, 2018.
- 1271 [59] P.K.F. Grieder. *Cosmic rays at Earth: researcher’s reference manual and data book*.
1272 Elsevier Science Ltd, Amsterdam, 1st ed edition, 2001.
- 1273 [60] R. Keyes et al. Development and characterization of a gas system and its associated
1274 slow-control system for an ATLAS small-strip thin gap chamber testing facility. *Journal
1275 of Instrumentation*, 12(04):P04027–P04027, April 2017.

- 1276 [61] Georgios Iakovidis. VMM3, an ASIC for Micropattern Detectors. Technical Report
1277 ATL-MUON-PROC-2018-003, CERN, Geneva, March 2018.
- 1278 [62] B. Chen. *Calibration Studies of the Front-End Electronics for the ATLAS New Small*
1279 *Wheel Project*. M.Sc. thesis, McGill University, Montreal, Canada, 2019.
- 1280 [63] R. Brun and F. Rademakers. ROOT: An object oriented data analysis framework. *Nu-*
1281 *clear Instruments and Methods in Physics Research Section A: Accelerators, Spectrome-*
1282 *ters, Detectors and Associated Equipment*, 389:81–86, 1997. See also ”ROOT” [software],
1283 Release 6.18/02, 23/08/2019, (<https://zenodo.org/record/3895860#.YVJW6n0pCHs>).
- 1284 [64] F. Sauli. Principles of operation of multiwire proportional and drift chambers. In *Cern*
1285 *Yellow Reports: Monographs*, page 92 p, Geneva, 1977. CERN, CERN. CERN, Geneva,
1286 1975 - 1976.
- 1287 [65] M. Hatlo et al. Developments of mathematical software libraries for the LHC experi-
1288 *ments. IEEE Transactions on Nuclear Science*, 52:2818–2822, 2005.
- 1289 [66] H. Guo. A Simple Algorithm for Fitting a Gaussian Function [DSP Tips and Tricks].
1290 *IEEE Signal Processing Magazine*, 28(5):134–137, September 2011.
- 1291 [67] B. Stelzer. The New Small Wheel Upgrade Project of the ATLAS Experiment. *Nuclear*
1292 *and Particle Physics Proceedings*, 273-275:1160–1165, April 2016.
- 1293 [68] X. Zhao et al. Cosmic test of sTGC detector prototype made in China for ATLAS
1294 experiment upgrade. *Nuclear Instruments and Methods in Physics Research Section A:*
1295 *Accelerators, Spectrometers, Detectors and Associated Equipment*, 927:257–261, May
1296 2019.

¹²⁹⁷ APPENDICES

1298 **Appendix A**

1299 **Uncertainty in cluster positions**

1300 **A.1 Cluster definition**

1301 A cluster is a series of contiguous strip channels on a layer with non-zero amplitude, all
1302 part of the same trigger and having the same event number [58]. Clusters result from the
1303 drift of ionization products generate in the ionization avalanche caused by a muon [54]. The
1304 peak-detector-output (PDO) of the signal on each strip of a cluster is fit with a Gaussian.
1305 The y-position of a particle as it passed through the layer is mean of the cluster, referred to
1306 here as the hit position.

1307 **A.2 Effect of fit algorithm on cluster mean**

1308 The clusters were fit with Guo's method [66] and Minuit2 for ROOT [65]. The difference in
1309 cluster means between the two algorithms is shown in figure A.1.
1310 The RMS of the distribution in figure A.1 is $57 \mu\text{m}$, which is much larger than the statistical
1311 uncertainty in the mean for the Minuit2 algorithm, which peaks around $7 \mu\text{m}$. An RMS of
1312 $60 \mu\text{m}$ is common for data taken with most quadruplets at 3.1 kV. Therefore, the uncertainty
1313 in the y-hit positions is assigned $60 \mu\text{m}$.

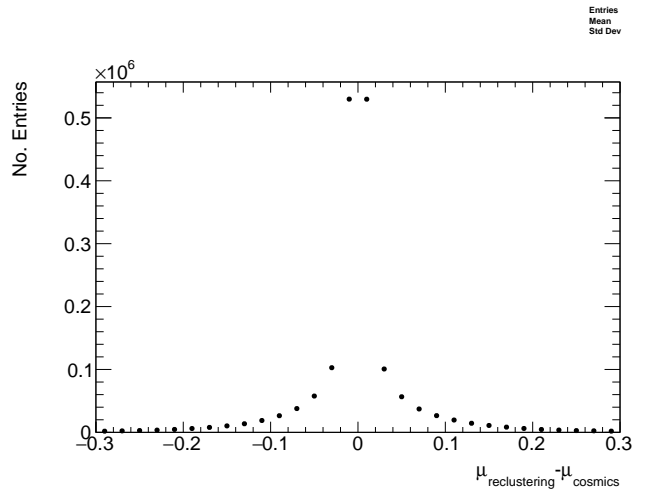


Figure A.1: The difference between cluster means calculated with Guo's method [66] in `tgc_analysis/CosmicsAnalysis` and `Minuit2` for `ROOT` [65] in `strip_position_analysis/ReClustering` for data collected with QL2.P.8 at 3.1 kV.

1314 **A.3 Effect of uncertainty in cluster mean on track residuals**

1315

1316 The uncertainty assigned to the hit position affected the uncertainty in the extrapolated/interpolated
1317 position of the track, and in the residuals. The bin size of the residual distributions was set
1318 to 200 μm because that was the uncertainty in the residuals calculated from the tracks with
1319 the least favourable geometry (like tracks built from hits on layers 1 and 2 and extrapolated
1320 to layer 4).

₁₃₂₁ **Appendix B**

₁₃₂₂ **Study of cosmics for alignment
1323 analysis statistical uncertainty**

₁₃₂₄ Typically, one million triggers (cosmic muon events, noise, photons and δ -rays) were collected
₁₃₂₅ for each Canadian quadruplet at McGill University, resulting in roughly half the number of
₁₃₂₆ viable tracks after cuts. For QS3.P.18, 3.5 million triggers were collected. To gauge the
₁₃₂₇ sensitivity of the analysis to the available statistics, partitions of this data with each with
₁₃₂₈ a different number of triggers were analyzed separately. Ultimately, the quantity of interest
₁₃₂₉ was the gaussian mean of the residual distribution in regions of interest, so the peak in the
₁₃₃₀ distribution of the statistical uncertainty in the residual means for each area of interest for
₁₃₃₁ a specific tracking combination was used to gauge the quality of the analysis. How the peak
₁₃₃₂ in the residual mean uncertainty distribution changes with the number of triggers is shown
₁₃₃₃ in figure for tracks on layer 1 built from layers 3 and 4 [B.1](#).

₁₃₃₄ The uncertainty is already around 20 μm at 1 million triggers, suitable for distinguishing
₁₃₃₅ differences in offsets of order 50 μm as required. Although increased statistics could decrease
₁₃₃₆ the statistical uncertainty, it is not required for the goals of this analysis. Moreoever, the
₁₃₃₇ systematic uncertainty is around 50 μm and the systematic uncertainty on the x-ray residuals
₁₃₃₈ is 150 μm so the statistical uncertainty of 20 μm is nearly negligible.

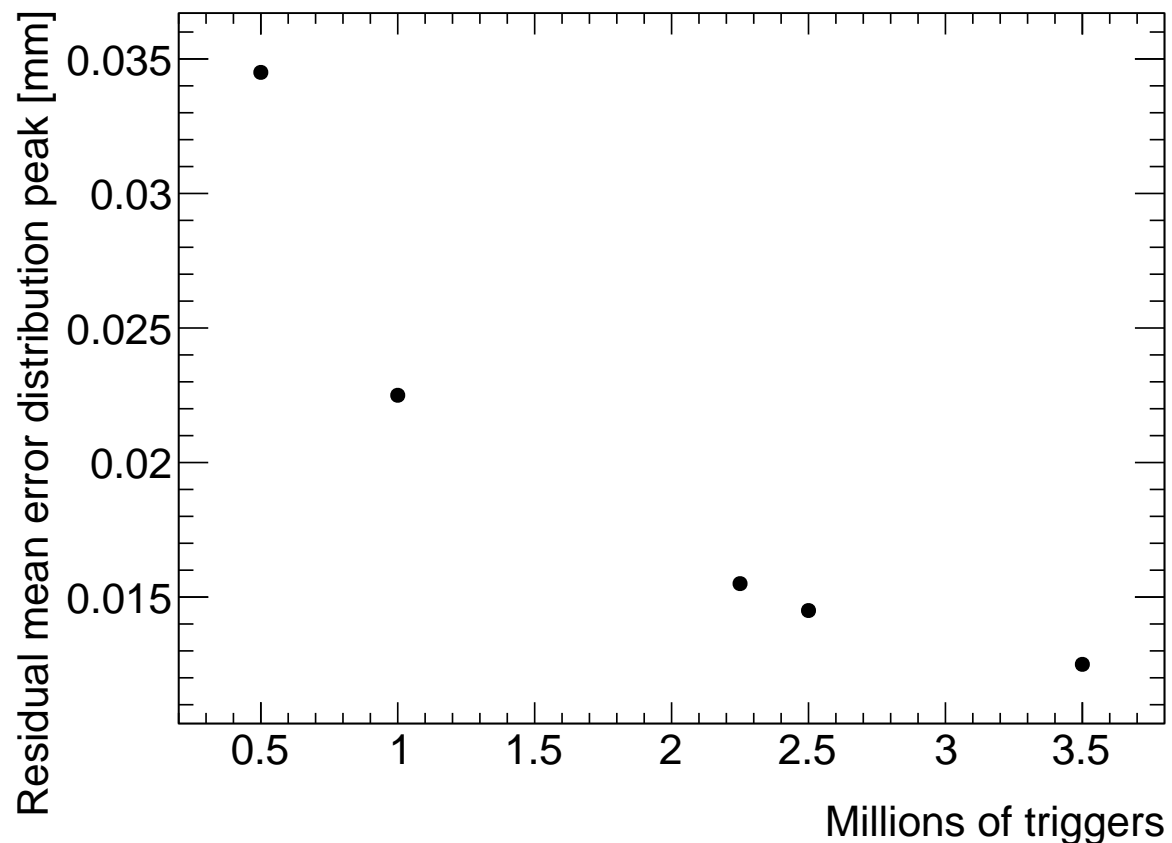


Figure B.1: How the peak of the distributions of uncertainties in the residual means in regions of interest for tracks on layer 1 built from layers 3 and 4 changed with the number of triggers used in the analysis. The distribution falls off as $\frac{1}{\sqrt{N}}$ as expected.

₁₃₃₉ **Appendix C**

₁₃₄₀ **Study of systematic uncertainties
when using cosmics data for
alignment studies**

₁₃₄₃ **C.1 Residual distribution fit function**

₁₃₄₄ The distribution of residuals should be modelled by a double gaussian fit[58]:

$$G(r) = A_s \exp\left[\frac{-(r - \mu)^2}{2\sigma_s^2}\right] + A_b \exp\left[\frac{-(r - \mu)^2}{2\sigma_b^2}\right] \quad (\text{C.1})$$

₁₃₄₅ where r is the residual, A is the gaussian amplitude, μ is the gaussian mean, σ is the
₁₃₄₆ gaussian sigma, and the subscripts s and b stand for signal and background respectively.
₁₃₄₇ One gaussian captures the real (signal) tracks and the other captures the tracks built from
₁₃₄₈ noise (background). The gaussian with the smaller width is identified as the signal.

₁₃₄₉ A single gaussian fit failed less often than a double gaussian fit. The gaussian fits were
₁₃₅₀ performed by initially estimating the amplitude to be 100 tracks, the gaussian mean to be
₁₃₅₁ the histogram mean, and gaussian σ to be the RMS. The fit range was restricted to ± 1 RMS
₁₃₅₂ from the histogram mean. The modification helped the gaussian fit capture the signal peak.
₁₃₅₃ An example residual distribution is shown in figure C.1.

₁₃₅₄ For all residual distributions in 100 mm by 100 mm bins on layer 4 built from hits on layers 1
₁₃₅₅ and 2, the difference in gaussian and double gaussian means and σ 's is shown in figure C.2.
₁₃₅₆ Since the RMS of the residual mean differences distribution is less than 50 μm the gaussian

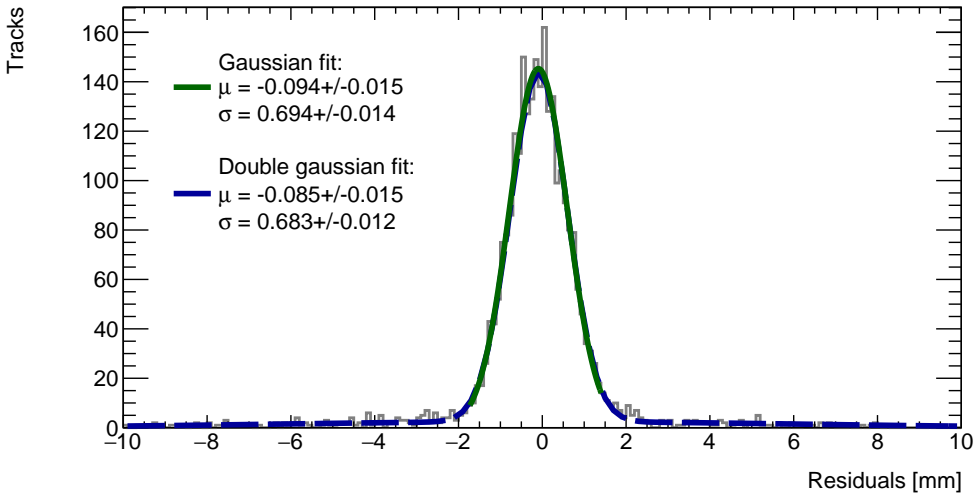


Figure C.1: Residual distribution for tracks on layer 4 built from hits on layers 1 and 2 for $x \in [-3.00, 97.00]$, $y \in [394.60, 494.60]$ mm for QL2.P.8 fit with a double gaussian and a single gaussian in a range of ± 1 RMS from the histogram mean.

1357 fit gave the same result within the required precision. Moreover, this is for the tracking
1358 combination with the worst extrapolation lever arm and the widest distribution of mean
1359 differences; the interpolation combinations have narrower distributions.

1360 The gaussian σ should be larger than the double gaussian σ because the gaussian distribution
1361 includes the effect of the noise tracks with large residuals, while the double gaussian models
1362 signal and background residuals separately. For this analysis, only the residual mean was
1363 important, so the systematic overestimate of the signal σ in the gaussian fit shown on the
1364 right of figure C.2 was allowed.

1365 C.2 Cosmic muon data collection voltage

1366 Cosmic muon data was collected at 2.9 kV and 3.1 kV because although 2.9 kV is closer to
1367 the operating conditions the chambers will be subject to in ATLAS, the extra gain provided
1368 by operating at 3.1 kV increased the signal to noise ratio for pad signals. Also, the tracking
1369 efficiency was higher with data collected at 3.1 kV. The difference in gain affected the relative
1370 population of clusters of different sizes, which in turn affected the uncertainty in the strip hit
1371 positions on each layer, the uncertainty in the track positions and the residual distributions.
1372 The residual distributions for 3.1 kV data are narrower, as shown in figure C.3.

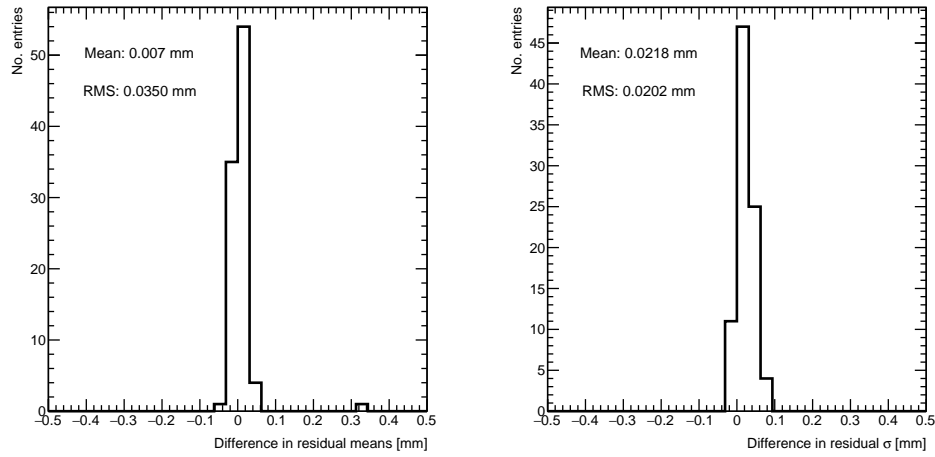


Figure C.2: Difference in residual distribution means and σ 's for a gaussian and double gaussian fit, for all residual distributions in 100 mm by 100 mm bins on layer 4 built from hits on layers 1 and 2 for QL2.P.8.

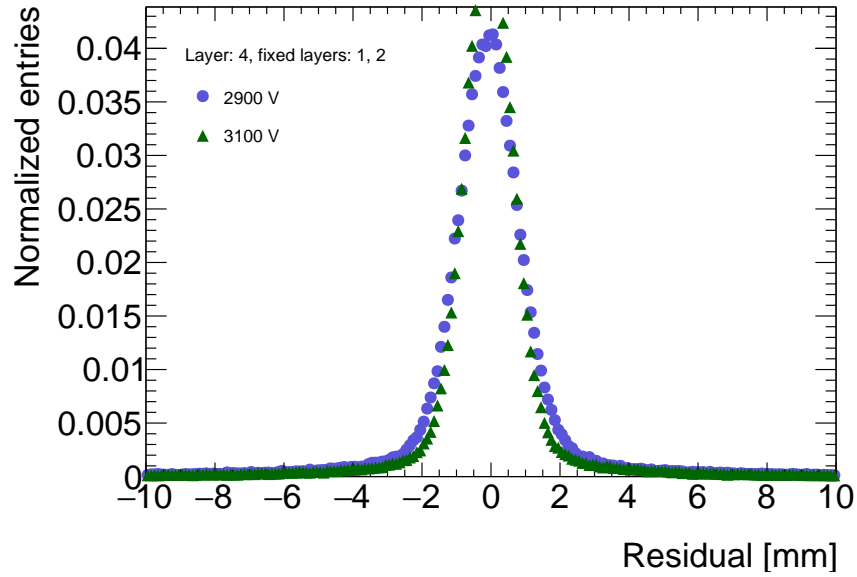


Figure C.3: Residual distribution for tracks on layer 4 built from hits on layers 1 and 2 for QL2.P.8 for data collected at 2.9 kV and 3.1 kV.

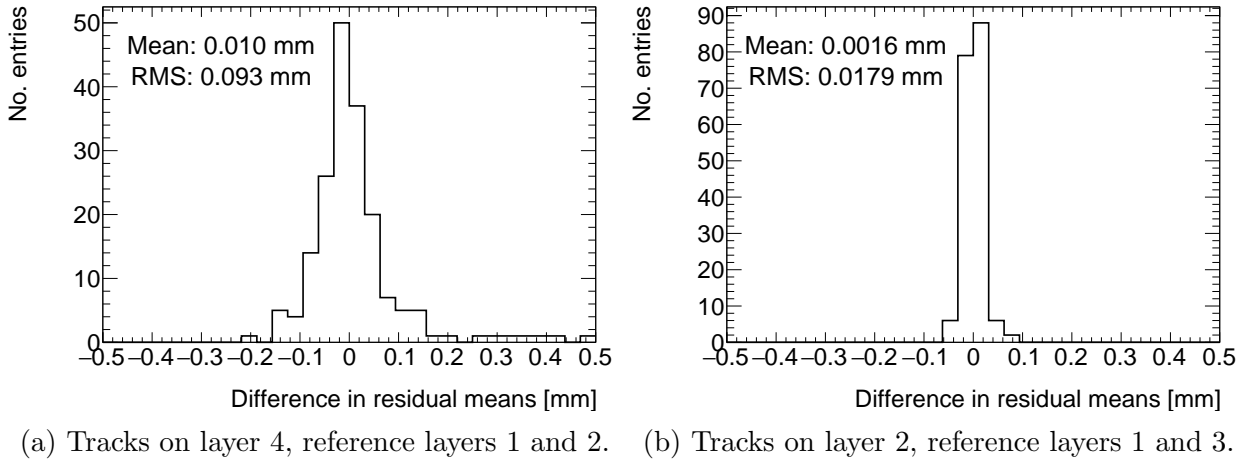


Figure C.4: Difference in residual means for data collected with QL2.P.8 at 2.9 kV and 3.1 kV respectively in 100 mm by 100 mm bins for (a) tracks on layer 4 built from hits on layers 1 and 2 and (b) tracks on layer 2 built from hits on layers 1 and 3.

1373 Neither dataset is better for calculating the mean of residuals in a given area, so a systematic
 1374 uncertainty can be assigned based on the difference in residual means calculated for 2.9 kV
 1375 and 3.1 kV data; namely, the systematic uncertainty was approximated as the RMS of the
 1376 residual mean difference distribution. Data taken with QL2.P.8 was used to estimate the
 1377 RMS, as in figure C.4a.

1378 Tracks built from hits on layers 1 and 2 and extrapolated to layer 4 have the worst lever arm
 1379 and hence the most uncertainty. The width of the distribution for geometrically favourable
 1380 tracks are much narrower. The narrowest width of the residual mean difference distribution
 1381 is for tracks on layer 2 built from hits on layers 1 and 3 (see figure C.4b).

1382 Therefore, for each tracking combination, a systematic uncertainty equal to the RMS of the
 1383 residual mean difference distribution was assigned.

1384 C.3 Cluster fit algorithm

1385 To ensure that changing the cluster fitting algorithm like in appendix A would not change
 1386 the calculated mean of residuals in each region of interest significantly, the residual means
 1387 were compared in both cases. The distribution of the difference in residual means is plotted
 1388 in figure C.5 for the tracking combination with the worst extrapolation lever arm.

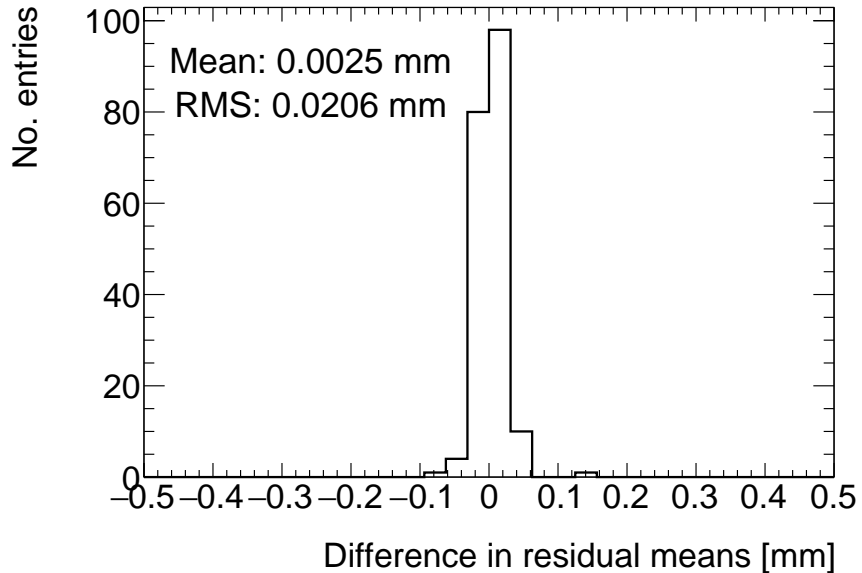


Figure C.5: Difference in residual means when the cluster fit algorithm is `Minuit2` [65] versus Guo’s method [66] for tracks on layer 4 built from hits on layers 1 and 2 for QL2.P.8.

1389 The other tracking combinations had smaller RMS values. Differences on the order of 50 μm
 1390 are important, so figure C.5 shows that the clustering algorithm had a small but notable
 1391 effect. Therefore, the RMS for each tracking combination will be used to add a systematic
 1392 uncertainty on the residual means.

1393 C.4 Differential non-linearity

1394 Definition

1395 In this context, differential non-linearity (DNL) is when the reconstructed cluster mean is
 1396 biased by the fit of the discretely sampled PDO distribution over the strips. The bias depends
 1397 on the relative position of the avalanche with respect to the center of the closest strip. For a
 1398 summary of DNL, refer to page 40 of Lefebvre’s thesis [58] and for an example application,
 1399 refer to [6].

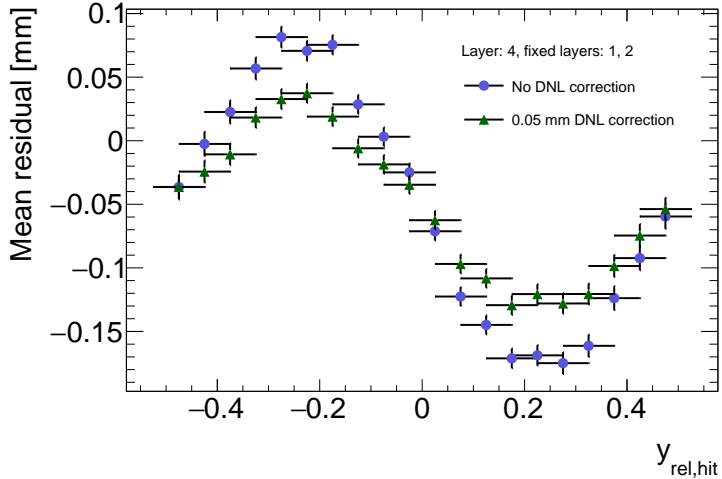


Figure C.6: Effect applying a 50 μm DNL correction to the cluster means on the residual vs y_{rel} distribution for tracks built from layers 1 and 2 and extrapolated to layer 4 for QL2.P.8.

1400 Application and effect of DNL

1401 The cluster mean was corrected for DNL using the equation:

$$y' = y + a \sin(2\pi y_{rel}) \quad (\text{C.2})$$

1402 where y is the cluster mean, y_{rel} is the relative position of the cluster mean with respect to
 1403 the strip's center, a is the amplitude of the correction, and y' is the corrected cluster mean.
 1404 The amplitude can be derived by comparing the reconstructed hit position to the expected
 1405 hit position, as done in Abusleme, 2016 [6]. With cosmic muons, there is no reference hit
 1406 position to compare to, so track residuals were used as a proxy [58]. The hallmark of the DNL
 1407 effect is the periodic pattern in the residual versus y_{rel} profile, and the effect of correcting
 1408 the cluster means using an amplitude of 50 μm is shown in figure C.6. An amplitude of
 1409 50 μm was based on Lefebvre's estimate of the DNL amplitudes by layer, quadruplet and
 1410 cluster size using exclusive cosmic muon tracks in `tgc_analysis/CosmicsAnalysis`. Little
 1411 variation was seen in the amplitude parameters with respect to the quadruplet tested, the
 1412 layer and the cluster size so a universal correction was used.

1413 Although the correction is not large enough in this case, the figure shows that the correction
 1414 does reduce the DNL effect. Slightly better performance is seen in the interpolation tracking
 1415 combinations where the quality of the residuals is better. DNL corrections for cosmic muon
 1416 data are difficult because the DNL effect is obscured by the effect of misalignments and

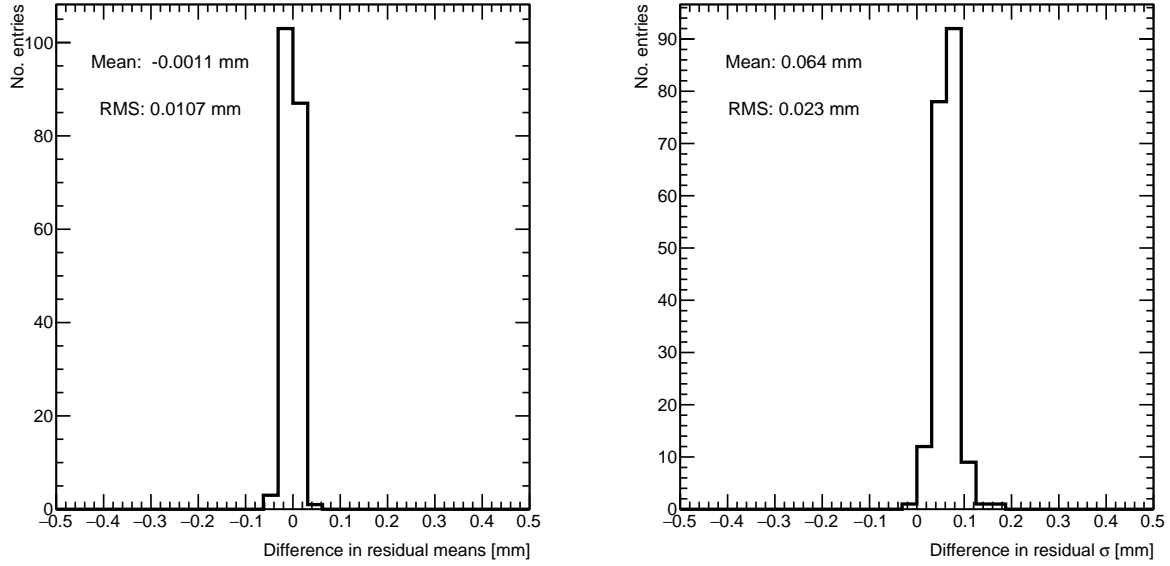


Figure C.7: Difference in residual distribution means and σ 's with and without DNL correction for residuals on layer 4 from reference layers 1 and 2 for QL2.P.8.

¹⁴¹⁷ noise. Misalignments cause the center of the sine pattern in figure C.6 to be shifted off of
¹⁴¹⁸ zero, since the mean of residuals is shifted.

¹⁴¹⁹ In figure C.7, it is apparent that the effect of the DNL correction on the mean of the
¹⁴²⁰ residual distribution in 100 mm by 100 mm areas is on the order of micrometers in the worst
¹⁴²¹ extrapolation case. Although the σ 's of the residual distributions shrink with the DNL
¹⁴²² correction, the mean is the parameter of interest. Therefore, for this analysis DNL was not
¹⁴²³ corrected for.

¹⁴²⁴ The σ 's of the residual distributions do shrink with the DNL correction but not so much to
¹⁴²⁵ affect the residual means, which are the important parameter for this analysis. Therefore,
¹⁴²⁶ since the effect of the DNL correction is negligible, it was not pursued further.

₁₄₂₇ Appendix D

₁₄₂₈ Printable plots

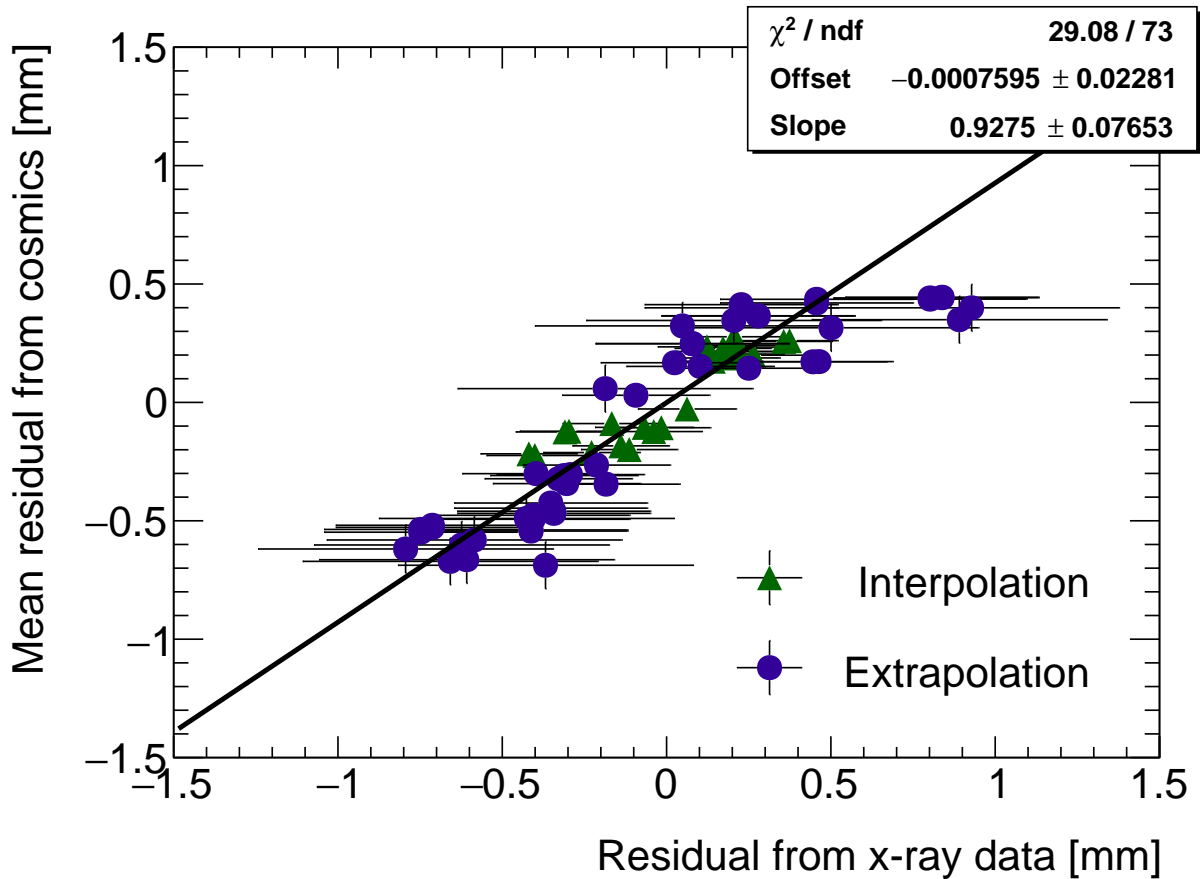


Figure D.1: Correlation plot between x-ray and cosmics residuals for all tracking combinations for QL2.P.11. Each rectangle is centered on an x-ray and mean cosmics residual pair. The width of the rectangles in x and y are the uncertainty in the x-ray and mean cosmics residual respectively. This is a printable version of figure 7.2 in section 7.1.

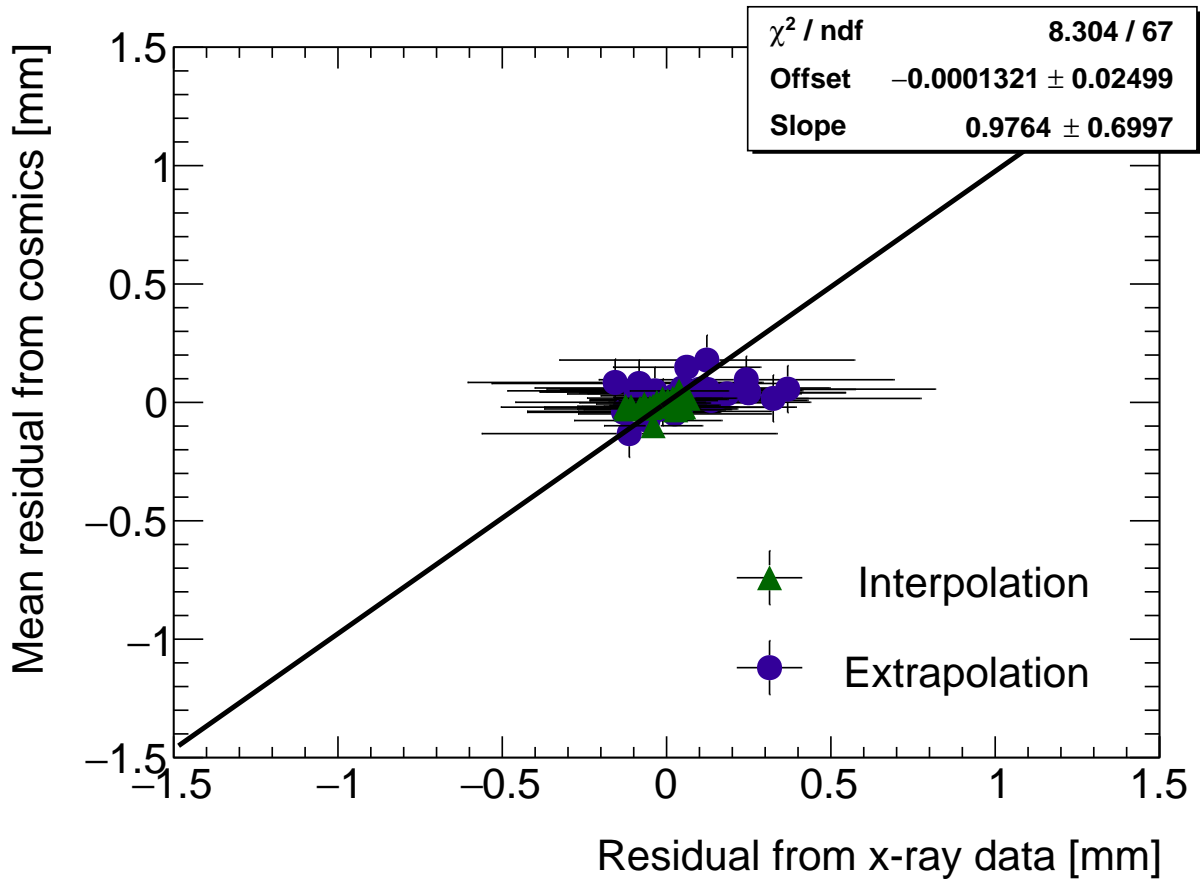


Figure D.2: Correlation plot between x-ray and cosmics residuals for all tracking combinations for QL2.P.8. Each rectangle is centered on an x-ray and mean cosmics residual pair. The width of the rectangles in x and y are the uncertainty in the x-ray and mean cosmics residual respectively. This is a printable version of figure 7.3 in section 7.1.